Bilateral regulation of EGFR activity and local PI dynamics observed with superresolution microscopy

Mitsuhiro Abe[1], Masataka Yanagawa[1,2], Michio Hiroshima[1,3], Toshihide Kobayashi[1,4], Yasushi Sako[1,*]

[1]Cellular Informatics Laboratory, RIKEN Cluster for Pioneering Research, Wako, Saitama 351-0198, Japan.

[2]Molecular and Cellular Biochemistry, Graduate School of Pharmaceutical Sciences, Tohoku University, 6-3, Aoba, Aramaki, Aoba-ku, Sendai, Miyagi 980-8578, Japan

[3]Laboratory of Single Molecule Biology, Graduate School of Frontier Biosciences, Osaka University, 1-3 Yamadaoka, Suita, Osaka 565-0871 Japan.

[4]Laboratoire de Bioimagerie et Pathologies, UMR 7021 CNRS, Université de Strasbourg, Faculté de Pharmacie, 67401 Illkirch, France.

* Corresponding author

Condensed title: Dynamics of PIP_2 nanodomains during EGFR signaling

Keywords: EGFR, membrane lipid, phosphatidylinositol-4,5-bisphosphate, superresolution microscopy, single-molecule imaging

Abstract

Anionic lipid molecules, including phosphatidylinositol-4,5-bisphosphate (PI(4,5)P_2), are implicated in the regulation of epidermal growth factor receptor (EGFR). However, the role of the spatiotemporal dynamics of PI(4,5)P_2 in the regulation of EGFR activity in living cells is not fully understood, as it is difficult to visualize the local lipid domains around EGFR. In this study, both EGFR and PI(4,5)P_2 nanodomains in the plasma membrane were visualized using super-resolution single-molecule microscopy. The EGFR and PI(4,5)P_2 nanodomains aggregated before stimulation with epidermal growth factor (EGF) through transient visits of EGFR to the PI(4,5)P_2 nanodomains. The degree of coaggregation decreased after EGF stimulation and depended on phospholipase Cγ, the EGFR effector hydrolyzing PI(4,5)P_2. Artificial reduction in the PI(4,5)P_2 content of the plasma membrane reduced both the dimerization and autophosphorylation of EGFR after stimulation with EGF. Inhibition of PI(4,5)P_2 hydrolysis after EGF stimulation decreased phosphorylation of EGFR-Thr654. Thus, EGFR kinase activity and the density of PI(4,5)P_2 around EGFR molecules were found to be mutually regulated.

Introduction

Epidermal growth factor receptor (EGFR) is a receptor tyrosine kinase responsible for cell proliferation and differentiation (Nyati et al., 2006; Olayioye et al., 2000). EGFR is subdivided into five regions: a large extracellular region, a single-spanning transmembrane I region, an intracellular juxtamembrane (JM) region, a tyrosine kinase region, and a C-terminal tail region (Lemmon et al., 2014). After EGFR binds to epidermal growth factor (EGF), the extracellular region adopts conformations favoring the dimerization of the transmembrane helices near their N terminus and the dimerization of the JM region (Arkhipov et al., 2013; Ogiso et al., 2002), inducing the formation of asymmetric (active) dimers of the intracellular kinase region (Red Brewer et al., 2009; Thiel and Carpenter, 2007; Zhang et al., 2006). This dimerization results in the phosphorylation of several tyrosine residues in the tail region and the recruitment of intracellular signal proteins, such as growth factor receptor-bound protein 2 (GRB2) and phospholipase Cγ (PLCγ) containing Src homology 2 (SH2) and/or phosphotyrosine-binding regions (Wagner et al., 2013). The JM region of EGFR plays a crucial role in the conformation-dependent coupling of EGFR's binding to EGF and its activation and dimerization (Endres et al., 2013; Jura et al., 2009b). The JM region comprises a JM-A (N-terminal half) region, which can form an antiparallel helix dimer, and a JM-B (C-terminal half) region, which makes intramolecular contact with the kinase region (Jura et al., 2009a). Both these JM regions contribute to the stable formation of an asymmetric kinase dimer, which is important for kinase activation.

Anionic lipid molecules in the inner leaflet of the plasma membrane are implicated in the dimerization of the JM regions (Hedger et al., 2015; Matsushita et al., 2013;

McLaughlin et al., 2005). Multiscale molecular dynamic simulations have suggested that phosphatidylinositol-4,5-bisphosphate (PI(4,5)P_2) interacts specifically with the basic residues in the JM-A region, stabilizing the JM-A helices in an orientation away from the membrane surface by binding to PI(4,5)P_2 (Abd Halim et al., 2015; Matsushita et al., 2013). In addition to these *in silico* analyses, our recent *in vitro* study using nanodisc techniques suggested that phosphatidylserine (PS) and PI(4,5)P_2 stabilize the conformation of the JM-A dimer (Maeda et al., 2018; Maeda et al., 2022). Apart from these *in silico* and *in vitro* studies, the localization and roles of PS and PI(4,5)P_2 during EGFR activation have not been fully investigated experimentally in living cells due to the difficulty of visualizing the local lipid domains around EGFR in the plasma membrane.

The main difficulty is that the proposed size of the lipid domain is below the diffraction limit of light. Therefore, conventional fluorescence microscopy cannot image the structure in detail. Superresolution imaging techniques that break the diffraction limit have become a powerful tool for visualizing cellular structures with unprecedented resolution (Pujals et al., 2019). Among these techniques, single-molecule localization microscopy (SMLM), which includes photoactivated localization microscopy, fluorescence photoactivation localization microscopy, stochastic optical reconstruction microscopy (STORM), ground-state depletion microscopy followed by individual molecular return, and direct STORM, allows the construction of superresolved images with high-precision localization of individual fluorophores (Rust et al., 2006).

In this study, we visualized both the EGFR and PI(4,5)P_2 nanodomains in the plasma membrane with SMLM. We found that the PI(4,5)P_2 nanodomains and EGFR

nanoclusters aggregate together before EGF stimulation. After stimulation, the degree of coaggregation decreases, which depends on PLCγ but not on phosphoinositide 3-kinase (PI3K). The local PI(4,5)P_2 around EGFR stabilizes EGFR dimers to increase EGFR autophosphorylation upon stimulation with EGF. The subsequent hydrolysis of PI(4,5)P_2 by PLCγ plays a crucial role in the deactivation of EGFR. Our results suggest that autogenous remodeling of the lipid environments regulates EGFR activity.

Results

EGF-induced reduction of PI(4,5)P_2 nanodomains

To visualize the nanodomains of EGFR and the lipids in the plasma membrane simultaneously, we constructed a three-color SMLM analysis workflow (see Methods, Fig. S1). EGFR was fused with rsKame, a slow-switching Dronpa variant (Rosenbloom et al., 2014), at the C-terminus. To exclude the effect of endogenous EGFR, we knocked out endogenous EGFR in HeLa cells, transfected them with EGFR–rsKame, and selected a cell line stably expressing the EGFR–rsKame fusion protein. When we stimulated the selected cell line with EGF, the EGFR–rsKame and extracellular signal-regulated kinase (ERK) in the cell line were phosphorylated to the same levels as in the parental HeLa cells (Fig. S2A and S2B), indicating that the EGFR–rsKame fusion protein functioned normally. To observe PI(4,5)P_2 with SMLM, the PI(4,5)P_2-binding peptide PLCδ-PH was fused with a photoactivatable protein, PAmCherry1 (Abe et al., 2012), and was transiently expressed in the cell line. To visualize PS with SMLM, the PS-specific peptide evectin-2 (evt-2)-PH (Uchida et al., 2011), tagged with HaloTag, was transiently expressed in the cell line, and was labeled with a spontaneous blinking dye, HMSiR (Takakura et al., 2017).

After the cells were fixed, sequential three-color SMLM was performed by imaging EGFR–rsKame illuminated with a 488-nm laser; PAmCherry1–PLCδ-PH (hereafter "PAmCherry–PI(4,5)P_2") activated with a 405 nm laser and illuminated with a 532 nm laser; and HMSiR–evt-2-PH (hereafter "HMSiR–PS") illuminated with a 637 nm laser (Fig. S1A). A single-molecule tracking analysis, drift correction, alignment of the color channels, image reconstitution, a multidistance spatial cluster analysis, and a G-function

spatial map (G-SMAP) analysis were then performed automatically according to the workflow shown in the Methods section.

EGFR–rsKame, PAmCherry–PI(4,5)P_2, and HMSiR–PS were distributed nonrandomly in the plasma membrane (Fig. 1A). The G-SMAP analysis revealed that EGFR, PI(4,5)P_2, and PS formed nanodomains with diameters ranging from <100 nm to several hundred nanometers. We measured the densities and areas of the nanodomains (Fig. 1B). Before EGF stimulation, their size was widely distributed, with a median of 0.0052 ± 0.0002 μm^2 (~0.04 μm radius, n = 8 cells) for the EGFR–rsKame nanodomains. Neither the density nor the area of the EGFR–rsKame nanodomains was affected by EGF stimulation (median of 0.0053 ± 0.0001 μm^2 in area, ~0.04 radius, n = 10 cells). However, the density of the PAmCherry–PI(4,5)P_2 nanodomains decreased after EGF stimulation; the median area of PAmCherry–PI(4,5)P_2 increased from 0.0049 ± 0.0001 μm^2 (~0.04 μm radius, n = 8 cells) to 0.0081 ± 0.0004 μm^2 (~0.05 μm radius, n = 10 cells, $p < 0.001$) after EGF stimulation. In particular, the size of smaller PAmCherry–PI(4,5)P_2 clusters was reduced after EGF stimulation.

We also analyzed the lateral univariate aggregation of the EGFR–rsKame, PAmCherry–PI(4,5)P_2, and HMSiR–PS molecules, calculating Ripley's univariate H-function, the derivative of Ripley's univariate K-function (Fig. 1C) that is frequently used in cluster analyses. The extent of aggregation, the H(r) value, was plotted as a function of the distance between molecules, r, in micrometers. The distance, r, that maximizes the H(r) value (referred to as the R value here) reflects the radius of the area in which the local density of molecules exceeds the random distribution by the largest amount (Kiskowski et

al., 2009). The R values of EGFR–rsKame, PAmCherry–PI(4,5)P_2, and HMSiR–PS were 0.20 ± 0.01 μm (n = 9 cells), 0.21 ± 0.01 μm (n = 9 cells), and 0.14 ± 0.01 μm (n = 10 cells), respectively (Fig. 1C). Therefore, the EGFR, PI(4,5)P_2, and PS molecules accumulated within membrane domains of similar sizes. The aggregations detected in the H-function analysis (~0.2 μm; Fig. 1C) were larger than those of the nanodomains estimated with the G-function-based clustering analysis of localization (~0.04 μm; Fig. 1B), indicating a hierarchical domain structure, that is, the formation of nanodomain clusters in the plasma membrane. The areas of aggregation (domain clusters) were not altered by EGF stimulation for 1 min. The R values for EGFR–rsKame, PAmCherry–PI(4,5)P_2, and HMSiR–PS were 0.20 ± 0.01 μm (n = 9 cells), 0.20 ± 0.01 μm (n = 9 cells), and 0.15 ± 0.01 μm (n = 9 cells), respectively. The peak H(r) value (referred to as the H(R) value here) indicates the degree of aggregation (Kiskowski et al., 2009). The H(R) value of EGFR–rsKame and HMSiR–PS was not significantly different before and after the addition of EGF (Fig. 1C, left and middle). However, after EGF stimulation, the H(R) value of PAmCherry–PI(4,5)P_2 decreased from 0.085 ± 0.006 to 0.043 ± 0.007 (n = 9 cells, $p < 0.001$; Fig. 1C, right).

Lateral coaggregation of EGFR and PI(4,5)P_2 decreases after EGF stimulation

EGFR and the lipid nanodomains partly colocalized in the plasma membrane (Figs. 1A and S2C). To estimate the degree of lateral coaggregation of the two different species of molecules, we calculated Ripley's bivariate H-function (Liu et al., 2023; Zhou et al., 2017). H(r) was plotted as a function of the distance r (Fig. 2A), between the two different species

of molecules. The peak value of bivariate H(r) (referred to as the bivariate H(R) value here) for EGFR–rsKame and HMSiR–PS was not significantly altered by EGF stimulation (Fig. 2A, left). The bivariate H(R) value of PAmCherry–PI(4,5)P_2 and HMSiR–PS also did not change significantly (Fig. 2A, middle). However, after EGF stimulation, the bivariate H(R) values of EGFR–rsKame and PAmCherry–PI(4,5)P_2 decreased from 0.0126 ± 0.0004 to 0.0066 ± 0.0005 (n = 8 cells, $p < 0.001$). Therefore, EGF stimulation reduced the coaggregation rate of this pair (Fig. 2A, right).

To confirm these results, we performed the following two experiments. First, we replaced PAmCherry–PI(4,5)P_2 with HMSiR–PI(4,5)P_2 and observed EGFR–rsKame and HMSiR–PI(4,5)P_2 with our SMLM system. EGF stimulation significantly reduced the bivariate H(R) value of EGFR–rsKame and HMSiR–PI(4,5)P_2 from 0.0133 ± 0.0010 (n = 17 cells) to 0.0027 ± 0.0003 (n = 20 cells, $p < 0.001$; Fig. 2B), similar to the results shown in Fig. 2A, right. Second, we observed EGFR–rsKame and HMSiR–GRB2 with our SMLM system and measured the bivariate H(R) value. EGF stimulation for 2 min increased the bivariate H(R) value of EGFR–rsKame and HMSiR–GRB2 from 0.0027 ± 0.0008 (n = 10 cells) to 0.0110 ± 0.0010 (n = 10 cells, $p < 0.001$; Fig. 2 C). These values are consistent with the finding that cytoplasmic GRB2 is recruited to phosphorylated EGFR after EGF stimulation (Yoshizawa et al., 2021). These two experiments support the idea that the H-function analysis of the SMLM data reflects the degree of coaggregation, and that EGF stimulation reduced the colocalization rate of EGFR and PI(4,5)P_2.

Because PI(4,5)P_2 and PI(3,4,5)P_3 have similar characteristics but play different roles in the plasma membrane (Insall and Weiner, 2001), we also examined the

coaggregation of EGFR and PI(3,4,5)P_3 before and after EGF stimulation. PAmCherry1–GRP1-PH (hereafter "PAmCherry–PI(3,4,5)P_3"), which specifically interacts with PI(3,4,5)P_3, was expressed in the EGFR–rsKame stable cell line (Fig. 2D) and the bivariate H(r) values of EGFR–rsKame and PamCherry–PI(3,4,5)P_3 were measured (Fig. 2E). The density of PamCherry–PI(3,4,5)P_3 was small with a low bivariate H(R) value before EGF stimulation. After EGF stimulation, the bivariate H(R) value was still low (Fig. 2E, red), although, consistent with a previous report (Malek et al., 2017), the number of PI(3,4,5)P_3 nanodomains stained with PamCherry–PI(3,4,5)P_3 increased (Fig. 2D). Thus, the nanodomains of PI(4,5)P_2 and PI(3,4,5)P_3 displayed distinct characteristics in their interactions with EGFR before and after EGF stimulation.

SMT analysis of EGFR and PI(4,5)P_2

Because the cells used in SMLM were artificially fixed with paraformaldehyde and glutaraldehyde, we examined the colocalization of EGFR and PI(4,5)P_2 in living cells (Figs. 3 and S3). After the EGFR–enhanced green fluorescent protein (EGFP) and Halo–PI(4,5)P_2 fusion proteins were expressed in EGFR-knockout (KO) HeLa cells, Halo–PI(4,5)P_2 was labeled with Janelia Fluor 549 (JF549). These proteins were observed with dual-color total internal reflection fluorescence for the single-molecule tracking (SMT) analysis (Fig. 3A). The movements of the fluorescent particles were classified into three motional modes (immobile, slow-mobile, and fast-mobile) according to their lateral diffusion coefficients (Hiroshima et al., 2018). The proportion of EGFR in the immobile fraction increased and the ratio in the fast-mobile fraction decreased after EGF stimulation

(Fig. 3B). The proportion of PI(4,5)P_2 in each fraction did not change significantly after EGF stimulation. The mean square displacement per unit time (MSD-Δt) of the lateral movements indicated that the diffusion coefficient of EGFR decreased after EGF stimulation, whereas that of PI(4,5)P_2 remained unchanged (Fig. S3A and S3B). All diffusion modes displayed subdiffusion. The confinement length of EGFR was also reduced after EGF stimulation, whereas that of PI(4,5)P_2 was not (Fig. S3C).

Next, we examined the colocalization of EGFR and PI(4,5)P_2. We found partial overlapping in the trajectory images of EGFR and PI(4,5)P_2 (Fig. 3C). Measurement of the colocalization rates revealed that EGFR–EGFP colocalized with Halo–PI(4,5)P_2 during 1.5% of the total observation periods before EGF stimulation (Fig. 3D). After EGF stimulation, the colocalization rate decreased to 1.0%. Among the three motional modes, the colocalization rate in the slow-mobile and fast-mobile fractions decreased after EGF stimulation, whereas the rate in the immobile fraction did not change significantly (Fig. S3D). These results confirm the results of SMLM, indicating that the colocalization rate decreased after EGF stimulation. The transient colocalization of EGFR and PI(4,5)P_2 was consistent with the small spatial overlapping of the nanodomains of these two molecular species in the SMLM images.

PI(4,5)P_2 is important for stabilizing the EGFR dimer

In silico and *in vitro* analyses have suggested that PI(4,5)P_2 is involved in the dimerization of EGFR (Abd Halim et al., 2015; Maeda et al., 2018; Maeda et al., 2022; Matsushita et al., 2013). The aggregation of PI(4,5)P_2 with EGFR in the plasma membrane

may help to stabilize the dimers of EGFR after its association with EGF. To test this, we reduced the content of PI(4,5)P_2 by expressing synaptojanin (SYNJ), a phosphatase that hydrolyzes PI(4,5)P_2, and we measured the size of the EGFR–Halo oligomer in CHO cells with an SMT analysis (Figs. 4A and S4A and S4B). Because dimerized EGFR was mainly found in the immobile fraction, we compared the oligomer size in the immobile fraction in SYNJ-expressing and control cells. SMT showed that fewer EGFR dimers formed in the SYNJ-expressing cells than in the control cells. Before EGF stimulation, 55.1 ± 2.6% (n = 40 cells) of EGFR particles were monomers, whereas 29.7 ± 0.8% (n = 40 cells) were preformed dimers in the control cells (Fig. 4A). After EGF stimulation, the monomer fraction decreased to 38.8 ± 4.1% (n = 40 cells) and the dimer fraction increased to 36.9 ± 1.8% (n = 40 cells) in the control cells. However, in the SYNJ-expressing cells, the monomer fraction decreased slightly even after EGF stimulation (57.6 ± 2.7% before and 50.3 ± 3.4% after EGF stimulation, n = 40 cells). The slow and fast fractions showed similar changes in EGFR as the immobile fraction. The mean density and mean intensity of EGFR–SF650 in the SYNJ-expressing cells before EGF stimulation were similar to those in the control cells, indicating that the expression levels of EGFR–SF650 were not significantly altered in SYNJ-expressing cells. These results suggest that PI(4,5)P_2 is important for stabilizing EGFR dimers after EGF stimulation.

Molecular dynamics simulations have shown that the conversion of three arginine residues to asparagine residues in the EGFR JM region (EGFR(3RN)) abolishes the interaction between EGFR and PI(4,5)P_2 (Abd Halim et al., 2015). Therefore, we examined the oligomer size of EGFR(3RN) in the immobile fraction (Figs. 4B, S5A, and S5B). The

monomer constituted 48.9 ± 2.5% of EGFR(3RN) (n = 45 cells) after EGF stimulation (Fig. 4B), which was similar to that in the SYNJ-expressing cells (Fig. 4A). The relative intensity of Cy5–EGF bound to EGFR did not differ significantly between EGFR(WT) and EGFR(3RN), suggesting that the 3RN mutation does not affect the binding of EGFR to EGF (Fig. S5C and S5D). These results suggest that the interaction of EGFR with PI(4,5)P_2 is important for the dimerization of EGFR.

We also measured the diffusion coefficient and the confinement length of EGFR in the immobile fraction (Fig. 4C and 4D). Because we saw no significant differences in the diffusion coefficients and confinement lengths in the SYNJ-expressing and control cells after stimulation with 100 nM EGF under our experimental condition, we measured them after stimulation with a low concentration of EGF (0.2 nM), which is below the dissociation constant of 2–6 nM (Sugiyama et al., 2023). The diffusion coefficient of EGFR in the immobile fraction after stimulation with 0.2 nM EGF was slightly higher in the SYNJ-expressing cells (0.0060 ± 0.0002 $\mu m^2/s$, n = 46 cells) than in the control cells (0.0051 ± 0.0002 $\mu m^2/s$, n = 46 cells, $p < 0.01$; Fig. 4C top). In the same fraction, the confinement length of EGFR was also slightly longer in the SYNJ-expressing cells (0.095 ± 0.002 μm, n = 46 cells) than in the control cells (0.089 ± 0.002 μm, n = 46 cells, $p < 0.05$; Fig. 4C, bottom). We also measured the diffusion coefficient and confinement length of EGFR(3RN) in the immobile fraction after stimulation with 0.2 nM EGF (Fig. 4D). As in the PI(4,5)P_2-depleted cells, the diffusion coefficient and confinement length of EGFR(3RN) in the immobile fraction (0.0096 ± 0.003 $\mu m^2/s$ and 0.106 ± 0.002 μm, respectively, n = 40 cells) were slightly higher than those of wild-type EGFR (EGFR(WT))

(0.0088 ± 0.002 $\mu m^2/s$ and 0.090 ± 0.003 μm, respectively, n = 40 cells). These results may reflect the formation of smaller numbers of dimers, which are less mobile than monomers, in PI(4,5)P_2-interaction depleted cells.

In SMT, molecular-level interactions of dimers cannot be detectable. Therefore, we confirmed these direct interactions with a biochemical analysis using a crosslinker (Fig. 5A and 5B). Cells were treated with 0.2 or 20 nM EGF, and cell-surface EGFR was crosslinked with EGFR using bis(sulfosuccinimidyl)suberate. The dimer fraction of EGFR was small before EGF stimulation but increased after stimulation with 0.2 or 20 nM EGF. Under both conditions, the expression of SYNJ reduced the amount of EGFR dimer (Fig. 5A and 5B), suggesting that PI(4,5)P_2 is involved in stabilizing the dimerization of EGFR.

Because the expression of SYNJ does not completely abolish PI(4,5)P_2 in the cell (Field et al., 2005), we could not determine whether PI(4,5)P_2 is essential for the dimerization of EGFR. To test this, we examined whether EGFR(3RN) forms dimers after EGF stimulation (Fig. 5C and 5D). After stimulation with 0.2 or 20 nM EGF, the amount of EGFR(3RN) dimers increased. If the interaction with PI(4,5)P_2 was not completely abolished in EGFR(3RN)-expressing cells, the amount of EGFR(3RN) dimers should decrease when PI(4,5)P_2 was reduced. There was no additive effect on the dimerization of EGFR(3RN) when SYNJ was expressed (Fig. 5C and 5D), suggesting that the interaction of EGFR(3RN) with PI(4,5)P_2 was rigorously blocked. Therefore, PI(4,5)P_2 is not essential for, but positively regulates EGFR dimerization.

The dimerization of EGFR leads to the phosphorylation of tyrosine residues in its tail region (Wagner et al., 2013). We examined whether the reduced dimerization of EGFR

under PI(4,5)P_2-interaction-depleted conditions resulted in defective phosphorylation of EGFR (Fig. 5E and 5F). The measurement of Tyr1068-phosphorylated EGFR after stimulation with 20 nM EGF indicated that the phosphorylation of EGFR decreased when SYNJ was overexpressed in cells. We also found that the Tyr1068 phosphorylation in EGFR(3RN) decreased relative to that in EGFR(WT) after stimulation with 20 nM EGF. However, after simulation with 0.2 nM EGF, no significant difference in the phosphorylation of EGFR was observed between the cells as EGFR was less phosphorylated under the current experimental conditions. These results confirm that PI(4,5)P_2 is important for not only the dimerization of EGFR but also its subsequent phosphorylation.

Extent of reduced coaggregation depends on PLCγ but not on PI3K

A biochemical analysis showed that the amount of PI(4,5)P_2 is transiently reduced after EGF stimulation in cells (Malek et al., 2017). Two kinds of enzymes are activated by EGFR and reduce the amount of PI(4,5)P_2 after EGF stimulation (Wells, 1999). First, PI3K phosphorylates PI(4,5)P_2 to produce PI(3,4,5)P_3 through dimerization of ERBB3 with EGFR (Hellyer et al., 1998). Second, phosphoinositide-specific PLCγ hydrolyzes PI(4,5)P_2 to produce diacylglycerol (DAG) and inositol trisphosphate (IP_3) through its direct physical association with EGFR via the SH2 regions of PLCγ (Carpenter and Ji, 1999). We investigated the protein responsible for the dissociation of EGFR from the PI(4,5)P_2 nanodomains after EGF stimulation. We inhibited either PI3K or PLCγ and measured the bivariate H(r) value of EGFR and PI(4,5)P_2 after EGF stimulation.

The addition of wortmannin, a PI3K inhibitor (Yano et al., 1993), diminished the PI3K-dependent phosphorylation of AKT after EGF stimulation (Fig. 6A). The expression of a dominant negative fragment of PLCγ containing the SH2, SH3, and PLC-inhibitory regions (referred to as "DN PLCγ" here) inhibits PLCγ activity (Banan et al., 2001; Homma and Takenawa, 1992). We found that the expression of DN PLCγ reduced DAG production after EGF stimulation compared with that in the non-DN-PLCγ-expressing control cells, indicating that the expressed fragment inhibited PLCγ activity (Fig. 6B).

Under these conditions, we observed EGFR and PI(4,5)P_2 in the plasma membrane with SMLM after EGF stimulation. To coexpress the PI(4,5)P_2 probe and DN PLCγ in the same cells, we used a plasmid containing an internal ribosome entry site (IRES). Measurement of Ripley's bivariate H-function revealed that no significant difference in the bivariate H(R) value of EGFR and PI(4,5)P_2 was observed between the wortmannin-treated (0.0102 ± 0.0010, n = 7 cells) and -untreated cells (0.0080 ± 0.0006, n = 7 cells), suggesting that PI3K is not important for the disaggregation of EGFR and PI(4,5)P_2 (Fig. 6C). However, the high bivariate H(R) value of EGFR and PI(4,5)P_2 was maintained in the DN-PLCγ-expressing cells (0.0225 ± 0.0015, n = 8 cells, $p < 0.001$) after EGF stimulation, suggesting that PLCγ is responsible for the reduced coaggregation of EGFR and PI(4,5)P_2 (Fig. 6C).

We examined whether EGFR activation is truly associated with its coaggregation with PLCγ by observing phosphorylated EGFR and PI(4,5)P_2 in the plasma membranes of wortmannin-treated or DN-PLCγ-expressing cells. After phosphorylated EGFR was immunostained with anti-EGFR (pY1068) and HMSiR-labeled antibodies in PAmCherry–

PI(4,5)P_2-expressing cells after EGF stimulation, the bivariate H(r) value of phospho-EGFR and PI(4,5)P_2 was measured (Fig. 6D). The bivariate H(R) values of phospho-EGFR and PI(4,5)P_2 in the control, wortmannin-treated, and DN-PLCγ-expressing cells were 0.0080 ± 0.0006 (n = 6 cells), 0.0093 ± 0.0010 (n = 7 cells), and 0.0193 ± 0.0012 (n = 8 cells), respectively. In the SMLM images of DN-PLCγ-expressing cells, overlapping of the nanodomains of phospho-EGFR and PI(4,5)P_2 was observed in the submicrometer coaggregation domains indicated in the bivariate H-function analysis (Fig. 6E).

We found that the univariate H(R) values of PI(4,5)P_2 were larger in the wortmannin-treated cells (0.071 ± 0.003, n = 9 cells) and DN-PLCγ-expressing cells (0.056 ± 0.005, n = 9 cells) than in the control cells (0.024 ± 0.002, n = 9; Fig. S6A). These results were expected from the inhibition of the metabolism of PI(4,5)P_2 in the wortmannin-treated and DN-PLCγ-expressing cells (Fig. 6A and 6B). Interestingly, the R value was smaller in the wortmannin-treated cells (0.131 ± 0.013 μm, n = 9 cells) than in the DN-PLCγ-expressing cells (0.252 ± 0.005 μm, n = 9 cells, Fig. S6A), suggesting that PI3K and PLCγ affect the PI(4,5)P_2 nanodomains in the plasma membrane differently. Consistent with these results, in the SMLM images, the nanodomains of PI(4,5)P_2 were more dispersed in the wortmannin-treated cells than in the DN-PLCγ-expressing cells (Fig. 6E). We detected no significant difference in the univariate H(R) values of pY1068 between the cells (Fig. S6B). These results support the conclusion that of the two enzymes PI3K and PLCγ, PLCγ mainly affects the reduction in the degree of coaggregation of EGFR and PI(4,5)P_2 after EGFR phosphorylation.

One possible explanation of the difference between the effects of these two enzymes

is that PLCγ hydrolyzes PI(4,5)P_2 bound to EGFR, whereas PI3K phosphorylates PI(4,5)P_2 far from EGFR in the plasma membrane. In EGFR KO and ERBB3 KO cells, no phosphorylation of AKT was detected after EGF stimulation (Fig. S6C and S6D). The expression of EGFR–Halo restored the phosphorylation of AKT after EGF stimulation in EGFR KO cells, but not in ERBB3 KO cells. Therefore, ERBB3 was required for the EGF-induced phosphorylation of AKT, supporting the possibility that PI3K phosphorylates PI(4,5)P_2 far from EGFR in the plasma membrane because ERBB3 mediates the activation of both EGFR and PI3K.

Hydrolysis of PI(4,5)P_2 by PLCγ is involved in the deactivation of EGFR

As shown in Fig. 6, we found that PLCγ is responsible for the reduced coaggregation of EGFR and PI(4,5)P_2 after EGF stimulation. PLCγ produces DAG, which is known to activate protein kinase C (PKC) (Steinberg, 2008). PKC activation is known to induce the phosphorylation of EGFR-Thr654 (Hunter et al., 1984), which is involved in the deactivation of EGFR. Therefore, we speculated that the hydrolysis of PI(4,5)P_2 around EGFR molecules by PLCγ upon EGF stimulation has a role in the deactivation of EGFR via PKC. To test this hypothesis, we measured the amount of Thr654-phosphorylated EGFR under PLCγ-inhibited conditions (Fig. 7A and 7B). We found that EGFR Thr654 was less phosphorylated in DN-PLCγ-expressing cells than in the control cells after EGF stimulation. The amount of Thr654-phosphorylated EGFR was also reduced in PLCG1-knockdown (KD) cells. The reduced phosphorylation of EGFR-Thr654 in PLCG1-KD cells was restored by adding 4β-phorbol 12-myristate 13-acetate (PMA), which is a DAG

mimetic (Fig. 7C and 7D), suggesting that the phosphorylation of Thr654 depends on DAG produced by PLCG1. Moreover, when the tyrosine kinase activity of EGFR was inhibited by AG1478, the phosphorylation of Thr654 was blocked in the control cells as well (Fig. 7C and 7D), which suggests that the phosphorylation of EGFR-Thr654 requires autophosphorylation of EGFR.

To exclude the possibility that the inhibition of PLCγ reduces the autophosphorylation of EGFR, we measured the phosphorylation of EGFR-Tyr1068 in DN-PLCγ-expressing and PLCG1-KD cells (Fig. 7A and 7B). Consistent with previous literature on mouse fibroblasts (Ji et al., 1998), the levels of Tyr1068-phosphorylated EGFR were not significantly altered in the DN-PLCγ-expressing or PLCG1-KD cells, suggesting that the inhibition of PLCγ does not block the kinase activity of EGFR. These results suggest that the autophosphorylation of EGFR activates PLCγ after EGF stimulation, inducing the phosphorylation of EGFR-Thr654 in a DAG-dependent manner.

Discussion

In this study, we examined the dynamics and functional roles of PI(4,5)P_2 as the boundary and/or neighboring lipid of EGFR in the activation of EGFR by EGF stimulation. Superresolution microscopy revealed that EGFR and PI(4,5)P_2 form nanodomains that partially overlap before EGF stimulation. The nanodomains also form domain clusters and the extent of coaggregation of EGFR and PI(4,5)P_2 molecules in a higher-order domain structure decreases after EGF stimulation. Single-molecule imaging confirmed these results, detecting the transient colocalization of EGFR and PI(4,5)P_2 in the immobile state. The expression of a PI(4,5)P_2 phosphatase reduced the dimerization and autophosphorylation of EGFR after EGF stimulation. These findings are consistent with previous *in vitro* and *in silico* observations that PI(4,5)P_2 interacts strongly with the arginine residues in the JM-A region of EGFR, stabilizing the active conformation of EGFR (Abd Halim et al., 2015; Matsushita et al., 2013). Together with these observations, our biochemical analyses suggest that the local distribution of PI(4,5)P_2 around EGFR before EGF stimulation not only acts as the substrate of EGFR effectors, including PI3K and PLCγ, after EGF stimulation, but also plays a crucial role in enhancing the dimerization and kinase activation of EGFR immediately after EGF stimulation (Fig. 7E, left).

We found that PI(4,5)P_2 is also involved in a specific pathway of EGFR deactivation after EGF stimulation. Tyr-phosphorylated EGFR recruits PLCγ, degrading PI(4,5)P_2 and producing DAG. DAG activates protein kinase C, which phosphorylates Thr654 of EGFR, deactivating EGFR (Fig. 7E, right). We have reported previously that Thr654 phosphorylation causes the JM-A dimer to dissociate in the presence of acidic lipids

(Maeda et al., 2018; Maeda et al., 2022). This constitutes the negative feedback regulation of the EGFR kinase function. Consistent with this, in our experiment, the expression of DN PLCγ did not induce DAG production (Fig. 6B) or Thr654 phosphorylation (Fig. 7A and 7B), but increased the Tyr1068 phosphorylation of EGFR (Fig. 7A and 7B). After the degradation of PI(4,5)P_2, EGFR is free from both positive and negative regulation by PI(4,5)P_2. We expect this state to facilitate the higher-order oligomerization of EGFR, which is important for signaling to cytoplasmic proteins (Hiroshima et al., 2018; Maeda et al., 2022).

We found that of PI3K and PLCγ, PLCγ is responsible for the disaggregation of the EGFR and PI(4,5)P_2 nanodomains after EGFR phosphorylation. A coaggregation analysis suggested that PLCγ hydrolyzes the local PI(4,5)P_2 around EGFR, whereas PI3K phosphorylates PI(4,5)P_2 in other pools in the plasma membrane. The presence of these two PI(4,5)P_2 pools suggests three possibilities. First, PI3K phosphorylates the PI(4,5)P_2 already present far from the activated EGFR before EGF stimulation because unlike PLCγ (Carpenter and Ji, 1999), PI3K is recruited indirectly through proteins associated with EGFR (Hellyer et al., 1998; Mattoon et al., 2004). Supporting this possibility, both EGFR and ERBB3 are required for the phosphorylation of AKT after EGF stimulation (Fig. S6C and S6D). The second possibility is that PI3K phosphorylates PI(4,5)P_2, which appears on the plasma membrane after EGF stimulation. It has been suggested that exocyst-mediated exocytosis is required for PI3K activation after EGFR phosphorylation (An et al., 2022). Because exocytosis transports recycling vesicles containing phosphatidylinositol-4-phosphate (PI(4)P) (Ketel et al., 2016), PI(4,5)P_2 may be synthesized from the PI(4)P

exocytosed at the plasma membrane after EGF stimulation. The small aggregation size of the PI(4,5)P_2 nanodomains observed in wortmannin-treated cells (Fig. S6A) may indicate that the PI3K associates with the PI(4,5)P_2 nanodomains that are newly synthesized at the plasma membrane after EGF stimulation. The inhibition of exocytosis should reveal the origin of the small PI(4,5)P_2 nanodomains observed in the wortmannin-treated cells. The third possibility is that the activity of PI3K that decreases the amount of PI(4,5)P_2 around EGFR molecules is lower than that of PLCγ. Further study is required to examine these possibilities.

We have shown here that the degree of coaggregation between EGFR and PI(4,5)P_2 is higher than that between EGFR and PS before EGF stimulation. The preferential coaggregation of the EGFR nanodomains with PI(4,5)P_2 rather than PS is probably due to the following two factors. The first is the curvature of the membrane. Previous electron microscopy–bivariate analyses showed that the nanodomains of inactive HRAS were enriched with PI(4,5)P_2, whereas those of active KRAS4B were enriched with PS due to highly specific RAS–lipid interactions determined by the membrane curvature (Liang et al., 2019; Zhou et al., 2014; Zhou et al., 2015). Like inactive HRAS, EGFR may prefer the PI(4,5)P_2 nanodomain environment, in addition to interacting electrostatically with PI(4,5)P_2. The second factor is tetraspanins, which form nanodomains at the plasma membrane. Tetraspanins may interact with EGFR and regulate EGFR activities and dynamics within tetraspanin nanodomains (Berditchevski and Odintsova, 2016; Odintsova et al., 2003; Sugiyama et al., 2023). Tetraspanins also interact indirectly with PI(4,5)P_2 (Halova and Draber, 2016). Therefore, EGFR may be localized in PI(4,5)P_2-enriched

nanodomains, mediated by tetraspanins.

PI(4,5)P_2 nanodomains may suppress EGFR signaling in the resting state despite their stabilizing effect on the JM-A dimer of EGFR during its kinase activation. Several reports have suggested that membrane cholesterol prevents EGFR phosphorylation before EGF stimulation (Chen and Resh, 2002; Ringerike et al., 2002). A biochemical analysis suggested that EGFR is associated with the detergent-resistant membrane fraction, which is enriched with cholesterol and PI(4,5)P_2 (Brown and London, 1998; Hope and Pike, 1996; Laux et al., 2000). We previously showed with SMLM that PI(4,5)P_2 nanodomains appear in the inner leaflet just beneath the sphingomyelin/cholesterol nanodomains located in the outer leaflet of the plasma membrane (Abe et al., 2012; Makino et al., 2017). Together with the results of the present study, this suggests that cholesterol- and PI(4,5)P_2-rich membrane domains exist in the plasma membrane, form higher-order aggregates, and transiently colocalize with EGFR clusters before EGF stimulation. Such membrane structures may prevent EGFR from activation because cholesterol exerts an inhibitory effect on EGFR. However, after EGF stimulation, rapid EGFR activation is induced by the positive effect of PI(4,5)P_2 on the dimerization of EGFR kinase. Transient complex of EGFR dimers with PI(4,5)P_2 may be required to leave the cholesterol nanodomains to allow kinase activation. The transient mobilization of EGFR clusters immediately after EGF stimulation that we have observed previously (Hiroshima et al. 2018) may reflect this process.

In conclusion, PI(4,5)P_2 plays a crucial role as a molecular switch for EGFR functions. PI(4,5)P_2 is involved in the complicated remodeling of the boundary lipids and higher-order membrane structure around EGFR. To detect whole these processes directly,

further observations are required using cholesterol and DAG probes under SMLM or electron microscopy. Alternatively, further biochemical analyses measuring the local lipid contents around EGFR should be performed.

Materials and Methods

Cell Culture and Drug Treatments

HeLa cells were grown at 37ºC in Dulbecco's modified Eagle's medium (DMEM) (Nacalai Tesque Inc., Kyoto, Japan) supplemented with 10% fetal bovine serum (FBS). CHO-K1 cells were grown at 37°C in Ham's F-12 medium (FUJIFILM Wako Pure Chemical Corporation, Osaka, Japan,) supplemented with 10% FBS.

Plasmid construction

DEST40/rsKame was generated by introducing V157L mutation into Dronpa in DEST40/Dronpa (Abe et al., 2012). The coding sequence for human EGFR was cloned into DEST40/rsKame, generating DEST40/EGFR-rsKame. The coding sequence for the human GRP1-PH region was obtained from HeLa cell cDNA by PCR amplification and cloned into DEST40/PAmCherry1, generating DEST40/PAmCherry-GRP1-PH. The coding sequence for the z region of human PLCγ (DN PLCγ) was cloned into DEST40 (Abe et al., 2012), generating DEST40/DN PLCγ. To generate DEST40/PAmCherry-PLCδ-PH-IRES-DN PLCγ, fragments of IRES and DN PLCγ were introduced just after PLCδ-PH in DEST40/PAmCherry-PLCδ-PH (Abe et al., 2012). EGFR–Halo was generated by replacing the fragment of EGFP in EGFR-EGFP (Hiroshima et al., 2018) with Halo7. Halo–PLCδ-PH and Halo–evt-2-PH were generated by replacing the fragment of Grb2 in Halo–Grb2 (Yasui et al., 2018) with PLCδ-PH and evt-2-PH, respectively. EGFR–Halo was generated by replacing the fragment of EGFP in EGFR-EGFP (Hiroshima et al., 2018) with Halo7. EGFR(3RN)–Halo was generated by introducing R645N/R646N/R647N mutations into EGFR in EGFR–Halo. EGFRvIII–Halo was generated by deleting 30-297 amino acids of EGFR in EGFR–Halo. To generate pTRE-EGFR-His, EGFR fused with 6xHis at the C-

terminus was cloned into the pTRE-Dual vector (TaKaRa Bio).

Generation of EGFR or ERBB3-KO cells with CRISPR/Cas9 gene editing

To construct the gene-editing plasmids, oligomers (5′-CACCGCACAGTGGAGCGAATTCCTT-3′ and 5′-AAACAAGGAATTCGCTCCACTGTGC-3′ for EGFR, 5′-CACCGTGATCCAGCAGAGAACCCAG-3′ and 5′-AAACCTGGGTTCTCTGCTGGATCAC-3′ for ERBB3) were synthesized, annealed, and cloned into the PX459 vector (#48139, Addgene) at the BbsI site, as previously described (Ran et al., 2013). HeLa cells were transfected with the resultant plasmid using Lipofectamine 3000 (Thermo Fisher Scientific, Waltham, MA). Single colonies were picked after selection with 0.3 μg/ml puromycin for 3 days. The genomic DNAs were extracted from the clones with the GenElute™ Mammalian Genomic DNA Miniprep Kit (Sigma-Aldrich, St. Louis, MO). The genome sequences were examined with PCR using the following primers: 5′-GATCGTGGACATGCTGCCTCCTGTGTCCATGACTGC-3′ and 5′-CTTCCCCTGCAGTATCTTACACACAGCCGGC-3′ for EGFR KO, or 5′-AGGTGGGGAAGGCATCTAGGGCAAAGGG-3′ and 5′-CGGAACTCGGGCGGTAATGCAAGTGATGG-3′ for ERBB3 KO cells. Sequence analysis revealed that the EGFR KO had a 1-bp deletion (C) next to the protospacer adjacent motif (PAM) sequence and that the ERBB3 KO had a 1-bp deletion (C) next to the PAM sequence.

Establishing cell lines stably expressing EGFR-rsKame

To establish cell lines stably expressing EGFR-rsKame, EGFR KO cells were transfected with DEST40/EGFR-rsKame by Lipofectamine 3000 (Thermo Fisher Scientific) and were cultured in the presence of 1 mg/ml G418 (Nacalai Tesque Inc.) for 14 days. Stable clones expressing EGFR-rsKame were selected and picked up under fluorescence microscopy.

Western blotting analysis

After EGFR-KO cells were transfected with EGFR(WT)–Halo, EGFR(WT)–Halo and mCherry–SYNJ, or EGFR(3RN)–Halo, cells were incubated in DMEM supplemented with 10% FBS for 24 h. The medium was replaced with DMEM supplemented with 0.2% bovine serum albumin (BSA), and cells were further incubated for 24 h. Cells were incubated with 0.2 nM or 20 nM EGF for 2 min and washed twice with cold PBS. After cells were lysed in ice-cold RIPA lysis buffer (Nacalai Tesque Inc.), lysates were cleared by centrifugation at 15,000 g for 10 min at 4°C. Proteins were separated on 4–15% TGX precast gels (Bio-Rad Laboratories Inc., Hercules, CA). Gels were transferred onto PVDF membranes using the Trans-Blot Turbo Transfer System and blocked with 2% non-fat dry milk in TBS + 0.1% Tween (TBST). Total EGFR was detected with anti-EGFR (#sc-3; Santa Cruz Biotechnology; 1:500) as a primary antibody and an HRP-linked anti-rabbit IgG (#7074, Cell Signaling Technology, Danvers, MA; 1:1000) as a secondary antibody. Immunoreactive proteins were detected with ECL Prime Western Blotting Detection Reagent (GE Healthcare) using an ImageQuant LAS 500 device (GE Healthcare). After the intensity of total EGFR was measured, we applied the proteins to SDS-PAGE again so that the intensity of total

EGFR in each sample was the same. Phosphorylated EGFR (pY1068) was detected with anti-EGFR pY1068 (#3777, Cell Signaling Technology; 1:1000) as a primary antibody and an HRP-linked anti-rabbit IgG. Total EGFR was detected as described above.

After EGFR-KO cells were transfected with EGFR–Halo, EGFR–Halo and DN PLCγ, or EGFR–Halo and PLCG1 siRNA (MISSION® siRNA, SASI_Hs02_00334210, Sigma-Aldrich) with Neon Transfection System (Thermo Fisher Scientific), cells were incubated in DMEM supplemented with 10% FBS for 24 h. The medium was replaced with DMEM supplemented with 0.2% BSA, and cells were further incubated for 24 h and stimulated with 10 nM EGF. For PMA treatment, cells were stimulated with EGF in the presence of 100 nM PMA. For inhibition of autophosphorylation of EGFR, cells were pretreated with 1 μM AG1478 for 30 min and stimulated with EGF. Phosphorylated EGFR (pT654) was detected with anti-EGFR pT654 (#ab75986; abcam, Cambridge, UK; 1:500) as a primary antibody and an HRP-linked anti-rabbit IgG. PLCG1 was detected with anti-PLCγ1 (#5690, Cell Signaling Technology; 1:500) as a primary antibody and an HRP-linked anti-rabbit IgG. Phosphorylated EGFR (pY1068) and total EGFR were detected as described above.

Parental HeLa cells and EGFR-KO cells stably expressing EGFR–rsKame fusion protein were incubated in serum-free medium overnight and stimulated with 20 nM EGF for 1 min. After cells were lysed, protein concentrations were determined with Pierce™ BCA Protein Assay Kits (Thermo Fisher Scientific). Proteins were applied to SDS-PAGE so that the protein concentrations were the same. Phosphorylated AKT (pS473) was detected with

anti-AKT (S473) (#4060, Cell Signaling Technology; 1:1000) as a primary antibody and an HRP-linked anti-rabbit IgG. Phosphorylated ERK (Thr202/Tyr204) was detected with anti-phospho-p44/42 (#4370, Cell Signaling Technology; 1:1000) as a primary antibody and an HRP-linked anti-rabbit IgG. Total ERK was detected with anti-p44/42 (#4695, Cell Signaling Technology; 1:1000) as a primary antibody and an HRP-linked anti-rabbit IgG.

Measurement of DAG

DN PLCγ was transiently expressed in a cell line stably expressing EGFR-rsKame. After cells were incubated in a serum-free medium overnight and treated with or without 20 nM EGF for 1 min. The amounts of DAG in the DN PLCγ-expressing and control cells were measured with a DAG assay Kit (#MET-5028, Cell Biolabs, Inc. San Diego, CA) according to manufacturer instructions.

Analysis of EGFR dimerization

After EGFR KO cells were transfected with the EGFR(WT)–Halo or EGFR(3RN)–Halo, cells were incubated in DMEM supplemented with 10% FBS for 24 h. The medium was replaced with DMEM supplemented with 0.2% BSA, and cells were further incubated for 24 h. Cells were incubated with 0.2 or 20 nM EGF for 2 min and washed twice with cold PBS. After cells were incubated in the presence of 3 mM BS3 (Thermo Fisher Scientific) in PBS at 4ºC for 1h, BS3 was quenched with 20 mM Tris-HCl (pH 8.0). Cells were washed twice with cold PBS. After cells were lysed, protein concentrations were determined. Proteins were subjected to western blotting analysis so that the protein concentrations were the same.

Cy5–EGF labeling

After EGFR-KO cells were transfected with EGFR(WT)–Halo, EGFR(3RN)–Halo, or EGFRvIII–Halo, cells were incubated in DMEM supplemented with 10% FBS for 24 h. The medium was replaced with DMEM supplemented with 0.2% BSA, and cells were further incubated for 24 h. Cells were stained with 10 nM Janelia Fluor® 549 (JF549) HaloTag Ligand (Promega, Madison, WI) for 30 min and were washed with the medium at least three times. After the medium was replaced with DMEM/Ham's F-12 containing HEPES and 0.2% BSA, 10 ng/mL Cy5–EGF was added as described (Sako et al., 2000). Confocal images were obtained within 10 min after Cy5–EGF with a confocal microscope (FV 3000, Olympus, Tokyo, Japan) equipped with a 60 × 1.35 NA objective lens.

Single-molecule tracking (SMT) analysis

An SMT analysis was performed as described previously (Kuwashima et al., 2021; Yanagawa et al., 2018; Yanagawa and Sako, 2021) with modifications. For SMT analysis of EGFR and PI(4,5)P_2, Hela cells were transfected with EGFR-EGFP and Halo–PLCδ-PH. After the cells were incubated in DMEM supplemented with 10% FBS for 24 h, the medium was replaced with DMEM supplemented with 0.2% BSA and the cells were further incubated for 24 h. Cells were stained with 10 nM JF549 for 30 min and were washed with DMEM/Ham's F-12 containing HEPES and 0.2% BSA but not Phenol Red at least three times. Single-molecule imaging in living cells was performed at room temperature (25 °C). The fluorescently labeled proteins were observed with the microscope (TiE, Nikon, Tokyo, Japan). The cells were illuminated with a 488-nm laser (OBIS 488, Coherent Inc., Santa Clara,

CA) and a 561-nm laser (OBIS 561, Coherent). The fluorescent images were recorded with Auto Imaging System (Zido, Osaka, Japan; http://zido.co.jp/en/) with an exposure time of 30 ms for dual-color imaging. The SMT and VB-HMM clustering analysis were performed with the Auto Analysis System (Zido) based on a two-dimensional Gaussian-fitting algorithm as described previously (Kuwashima et al., 2021; Yanagawa et al., 2018; Yanagawa and Sako, 2021). All subsequent analyses (diffusion dynamics, intensity distribution, colocalization, and statistical analysis) were performed using an updated version of smDynamicsAnalyzer, an Igor Pro 9.0, WaveMetrix (Igor)-based homemade program. Refer to the reference for the detailed instruction and curve fitting functions (Yanagawa and Sako, 2021).

For SMT analysis of EGFR and EGFR(3RN), CHO-K1 cells were transfected with EGFR–Halo, EGFR–Halo and DEST40/mCherry-SYNJ (Abe et al., 2012), or EGFR(3RN) –Halo and incubated in Ham's F-12 supplemented with 10% FBS for 24 h. After the medium was replaced with DMEM supplemented with 0.2% BSA, cells were further incubated for 24 h. Cells were stained with 1 nM SaraFluor™ 650T Ligand (#A308-01, GORYO Chemical, Inc. Sapporo, Japan) for 30 min and were washed with DMEM/Ham's F-12 containing HEPES and 0.2% BSA but not Phenol Red at least three times. The fluorescently labeled proteins were observed with the microscope (TiE, Nikon, Tokyo, Japan) as described above with a 637-nm laser (OBIS 637, Coherent Inc.). The fluorescent images were recorded as described above.

SMLM imaging

Cell lines stably expressing EGFR-rsKame were transfected with the plasmids by

Neon Transfection System (Thermo Fisher Scientific). After 1 day, the cells were incubated with 10 nM HaloTag HMSiR Ligand (#A201-01, GORYO Chemical, Inc.) in DMEM supplemented with 0.2% BSA for 16 h. Cells were washed with fresh medium and further incubated for 3 h. Cells were fixed with 4% paraformaldehyde and 0.2% glutaraldehyde for 60 min and washed with PBS. To calibrate the drift, TetraSpeck™ Microspheres (#T7279; Thermo Fisher Scientific) was added before observation. EGFR-rsKame on the basal plasma membrane was illuminated with a 488-nm laser (OBIS 488, Coherent) and observed with total internal reflection illumination with an inverted fluorescence microscope (TiE, Nikon). PAmCherry was photoactivated with a 405-nm (COMPASS 405-25 CW, Coherent) and illuminated with a 532-nm laser (COMPASS 315M-100, Coherent). HMSiR was illuminated with a 637-nm laser (OBIS 637, Coherent). 1000 frames of the fluorescent images were acquired with the Auto Imaging System (Zido, Japan) at a frame rate of 30 ms.

For staining of phosphorylated EGFR, cells were fixed with 4% paraformaldehyde and 0.2% glutaraldehyde for 60 min. The cells were permeabilized with 0.1% Triton X-100 in PBS and were blocked with 2% BSA for 1 h. Then, the cells were incubated with anti-EGFR pY1068 (#3777, Cell Signaling Technology; 1:100) for 1 h. The cells were washed and incubated with HMSiR-coupled goat anti-rabbit IgG (#A204-01, GORYO Chemical, Inc.).

SMLM analysis workflow

All subsequent analyses (image reconstitution, automated multi-distance spatial clustering analysis, G-SMAP analysis, and statistical analysis) were performed using an

updated version of smDynamicsAnalyzer. See the legend for Fig. 1S and Yanagawa and Sako, 2021 for the details of SMLM analysis workflow.

Localizations of single-fluorophore-labeled proteins (samples) and TetraSpeck™ Microspheres (beads) were determined by 2D Gaussian fitting algorism. Thermal drift and misalignment between color channels were corrected by an affine transformation using the localizations of the beads as indices (Fig. S1 B). The positional accuracy of the immobile fluorescence beads was estimated to be 6-8 nm (full width at half maximum, FWHM) (Figs. S1B and S2D). The positional accuracy of the single molecules was typically 20-30 nm. The accuracy of the superimposition of two images after the affine transformation was 10-14 nm (Figs. S1B and S2E).

SMLM images were reconstituted by convolving 2D-Gaussian functions for the single-molecule images (Fig. S1C). To avoid multi-counting of the same molecule, the positions of a single-molecule were averaged and plotted at a single location. The image resolution of SMLM was estimated with a method based on Fourier ring correlation (FRC) (Nieuwenhuizen et al., 2013). Resolution values for Dronpa(V157L), PAmCherry1, and HMSiR were 30.1 ± 2.9 nm, 26.8 ± 1.2 nm, and 28.2 ± 1.0 nm, respectively (means ± SEM, n = 5).

We developed and used a multi-distance spatial cluster analysis program to estimate the size and distribution of nano-domains automatically (Fig. S1D-S1F), where the local point density around each point was compared with that for the random distribution based on the Ripley's K-function, K(r), and its variants for cluster analysis (Kiskowski et al., 2009) and co-cluster analysis (Lagache et al., 2018). We also generated a G-function

spatial map (G-SMAP) to visualize single clusters (Fig. S1 F). The size of each cluster, the number of points within each cluster, and the point density in a cluster were calculated in the G-SMAPs.

Statistical analysis

Statistical significance was determined using Welch's t-test between groups. We considered P-values < 0.05 to be statistically significant, and classified them into the following 4 categories: * ($p < 0.05$), ** ($p < 0.01$), *** ($p < 0.001$), and NS (not significant, i.e., $p \geq 0.05$).

Online supplemental materials

Fig. S1 shows the multicolor SMLM analysis workflow. Fig. S2 shows the construction and evaluation of multicolor SMLM. Fig. S3 shows SMT analysis of EGFR–EGFP and JF549–PI(4,5)P_2. Fig. S4 shows SMT analysis of EGFR under PI(4,5)P_2-depleted condition. Fig. S5 shows SMT analysis of EGFR under PI(4,5)P_2-interaction-depleted condition. Fig. S6 shows that PI3K is not responsible for EGFR dissociation from PI(4,5)P_2 nanodomains after EGFR is phosphorylated.

Data availability

The raw data and code are available from the corresponding author upon reasonable request.

Acknowledgments:

This work was supported by Grants-in-Aid from the Ministry of Education, Culture, Sports, Science, and Technology of Japan (22K06609 to M.A, 19H05647 to Y.S.); Japan Science and Technology Agency (JST), PRESTO, JPMJPR20EF (M,Y); and the Glycolipidologue Program of RIKEN (to Y.S. and T.K). We thank Dr. Ryo Maeda for the technical advice for biological experiments. We also thank Maiko Minatohara for biochemical experiments. We thank the Support Unit for Bio-Material Analysis, RRD, RIKEN for DNA sequence and cell sorting.

Author contributions: M.A., M.Y., and Y.S. designed the experiments. M.H., M.Y., and Y.S. developed the microscope station. M.Y. developed the software for SMLM and SMT. M.A. performed the biological experiments. M.A. and T.K. designed and made the lipid probes. M.A. and M.Y. performed SMLM and SMT experiments and data analysis. M.A., M.Y., and Y.S. wrote the manuscript with input from all co-authors.

Figure legends

Figure 1 Size and distribution of nanodomains of EGFR, PI(4,5)P_2, and PS.

(**A**) Images of EGFR–rsKame (cyan), PAmCherry–PI(4,5)P_2 (magenta), and HMSiR–PS (yellow) before EGF stimulation. PAmCherry–PI(4,5)P_2 and Halo–evt-2-PH (Halo–PS) were transiently expressed in a cell line stably expressing EGFR–rsKame. Cells were incubated in serum-free medium in the presence of the HMSiR–Halo ligand overnight and treated with paraformaldehyde and glutaraldehyde. Left, a typical image of 15 × 15 μm. Right, enlarged image of the square region surrounded by a bold line in the left image. Enlarged images of other square regions surrounded by thin lines in the left image are shown in Fig. S2C.

(**B**) Distribution of the densities of EGFR (left) and PI(4,5)P_2 cluster areas (right). Cells were incubated in serum-free medium overnight, stimulated with or without 20 nM EGF for 1 min, and treated with paraformaldehyde and glutaraldehyde. From the SMLM images, the cluster areas and the number of clusters were measured. After the cluster number was normalized to the cell area (density), the cluster density was plotted as a function of the cluster area. Inset, enlarged graphs for the cluster areas of <0.03 μm^2. Blue and red indicate before and after EGF stimulation, respectively. Data are means ± SEM of eight cells.

(**C**) Univariate H(R) values of EGFR–rsKame (left), PAmCherry–PI(4,5)P_2 (middle), and HMSiR–PS (right) in cells incubated in the absence (blue) or presence (red) of 20 nM EGF for 1 min. Ripley's univariate H-function was calculated from the SMLM images. Data are means ± SEM of nine (EGFR–rsKame and PAmCherry–PI(4,5)P_2) or 10 (HMSiR–PS) cells.

Figure 2 Bivariate H(r) calculated from SLML images.

(**A**) Bivariate H(r) value of EGFR–rsKame and HMSiR–PS, PAmCherry–PI(4,5)P_2 and HMSiR–PS, and EGFR–rsKame and PAmCherry–PI(4,5)P_2 before (blue) and after incubation with 20 nM EGF for 1 min (red). Cells were prepared as in Fig. 1. Ripley's

bivariate H-function was calculated from the SMLM images. Data are means ± SEM of eight cells.

(**B**) Bivariate H(r) value of EGFR–rsKame and Halo–PI(4,5)P_2 before (blue) and after incubation with 20 nM EGF for 2 min (red). Halo–PI(4,5)P_2 was transiently expressed in a cell line stably expressing EGFR–rsKame. Cells were incubated in serum-free medium in the presence of the HMSiR–Halo ligand overnight, stimulated with or without 20 nM EGF for 2 min, and treated with paraformaldehyde and glutaraldehyde. Data are means ± SEM of 17 (without EGF stimulation) or 20 cells (with 20 nM EGF stimulation).

(**C**) Bivariate H(r) value of EGFR–rsKame and Halo–GRB2 before (blue) and after incubation with 20 nM EGF for 2 min (red). Halo–GRB2 was transiently expressed in a cell line stably expressing EGFR–rsKame. Cells were prepared as described in (B). Data are means ± SEM of 10 cells.

(**D**) Images of EGFR–rsKame (cyan) and PAmCherry–PI(3,4,5)P_3 (magenta) before (left) and after EGF stimulation for 2 min (right). PAmCherry1–GRP1-PH (PAmCherry–PI(3,4,5)P_3) was transiently expressed in a cell line stably expressing EGFR–rsKame. Cells were prepared as described in (B).

(**E**) Bivariate H(r) value of EGFR–rsKame and PAmCherry–PI(3,4,5)P_3 before (blue) and after incubation with 20 nM EGF for 2 min (red). Data are means ± SEM of 10 (before EGF stimulation) or nine cells (after 20 nM EGF stimulation).

Figure 3 Lateral coaggregation of EGFR and PI(4,5)P_2 decreases after EGF stimulation.

SMT analysis of EGFR–EGFP and JF549–PI(4,5)P_2 (A)-(D). (**A**) Trajectories of EGFR–EGFP (left) and JF549–PI(4,5)P_2 (right) over 6 s. EGFR–EGFP and Halo–PLCδ-PH (Halo–PI(4,5)P_2) were transiently expressed in EGFR-KO HeLa cells. After the cells were incubated in serum-free medium overnight, Halo–PI(4,5)P_2 was stained with JF549–Halo

ligand. EGFR–EGFP and JF549–PI(4,5)P_2 were observed in 32 cells at a time resolution of 30 ms for 6 s before EGF stimulation. After stimulation with 20 nM EGF, EGFR–EGFP and JF549–PI(4,5)P_2 were observed in the same cells between 1 and 5 min after the addition of EGF. SMT analysis was fractionated into the immobile (blue), slow-mobile (yellow), and fast-mobile (green) fractions.

(**B**) Proportions of immobile (blue), slow-mobile (yellow), and fast-mobile (green) fractions.

(**C**) Trajectories of EGFR–EGFP (green) and JF549–PI(4,5)P_2 (magenta) during 6 s before (left) and after incubation with 20 nM EGF (right).

(**D**) Colocalization rate of EGFR–EGFP and JF549–PI(4,5)P_2 before and after incubation with 20 nM EGF. ***$p < 0.001$ on Welch's *t* test.

Figure 4 SMT analysis of EGFR–Halo in control and SYNJ-expressing cells

EGFR–Halo was transiently expressed in CHO-K1 cells. After cells were incubated in serum-free medium overnight, EGFR–Halo was stained with the SF650–Halo ligand. EGFR–SF650 was observed in control (n = 40) and SYNJ-expressing cells (n = 40) at a time resolution of 30 ms before EGF stimulation. Following stimulation with 100 nM EGF, EGFR–SF650 was observed in the same cells between 1 and 6 min after the addition of EGF.

(**B**) SMT analysis of EGFR(WT)–Halo and EGFR(3RN)–Halo. EGFR–Halo or EGFR(3RN)–Halo was transiently expressed in CHO-K1 cells. After the cells were incubated in serum-free medium overnight, EGFR–Halo was stained with the SF650–Halo ligand. EGFR(WT)–SF650 (n = 40) and EGFR(3RN)–SF650 (n = 45) were observed as described in (A). Data are means ± SEM.

(**C**) Diffusion coefficient (top) and confinement length (bottom) of EGFR–SF650 in the immobile fraction. EGFR–Halo was transiently expressed in CHO-K1 cells. After the cells

were incubated in serum-free medium overnight, EGFR–Halo was stained with the SF650–Halo ligand. EGFR–SF650 was observed in control and SYNJ-expressing cells (n = 46) at a time resolution of 30 ms before EGF stimulation. Following stimulation with 0.2 nM EGF, EGFR–SF650 was observed in the same cells between 1 and 6 min after the addition of EGF.

(**D**) Diffusion coefficients (top) and confinement lengths (bottom) of EGFR(WT)–SF650 and EGFR(3RN)–SF650 in the immobile fraction. EGFR(WT)–Halo or EGFR(3RN)–Halo was transiently expressed in CHO-K1 cells. After the cells were incubated in serum-free medium overnight, EGFR–Halo was stained with the SF650–Halo ligand. EGFR(WT)–SF650 and EGFR(3RN)–SF650 were observed in cells (n = 40) at a time resolution of 30 ms before EGF stimulation. Following stimulation with 0.2 nM EGF, EGFR(WT)–SF650 and EGFR(3RN)–SF650 were observed in the same cells between 1 and 6 min after the addition of EGF. *$p < 0.05$, **$p < 0.01$, ***$p < 0.001$ on Welch's *t* test.

Figure 5 Biochemical analysis of EGFR under PI(4,5)P_2-depleted conditions.

(**A**) Western blotting analysis of crosslinked EGFR. After EGFR-KO cells were transfected with only EGFR–Halo or both EGFR–Halo and EGFP–SYNJ, the cells were incubated in serum-free medium overnight. The cells were then stimulated with 0, 0.2, or 20 nM EGF, and treated with a crosslinker for 1 h. EGFR–Halo was detected with an anti-EGFR antibody.

(**B**) Amounts of EGFR–Halo dimer. Relative intensity was normalized to the mean intensity of lane #3 in (A). Data are means ± SD of four experiments.

(**C**) Western blotting analysis of crosslinked EGFR(3RN). After EGFR-KO cells were transfected with only EGFR(3RN)–Halo or both EGFR(3RN)–Halo and EGFP–SYNJ, the cells were incubated in serum-free medium overnight. The cells were then stimulated with 0.2 or 20 nM EGF, and treated with a crosslinker for 1 h. EGFR(3RN)–Halo was detected with an anti-EGFR antibody.

(**D**) Amounts of EGFR(3RN)–Halo dimer. Relative intensity was normalized to the mean

intensity of lane #1 in (C). Data are means ± SD of three experiments.
(**E**) Western blotting analysis of phosphorylated EGFR and total EGFR. After EGFR-KO cells were transfected with EGFR(WT)–Halo, EGFR(WT)–Halo and mCherry–SYNJ, or EGFR(3RN)–Halo, the cells were incubated in serum-free medium overnight and stimulated with 0.2 nM or 20 nM EGF for 2 min. Phospho-EGFR and total EGFR were detected with anti-pY1068 EGFR and EGFR, respectively.
(**F**) Ratio of phosphorylated-Tyr1068 EGFR/total EGFR. The ratio was normalized to the mean value of lane #4 in (E). Data are means ± SD of three experiments. *$p < 0.05$, **$p < 0.01$, NS (not significant) on Welch's *t* test.

Figure 6 PLCγ is responsible for EGFR dissociation from PI(4,5)P_2 nanodomains after EGFR is phosphorylated.

(**A**) Effect of wortmannin on phosphorylation of AKT. A cell line stably expressing EGFR–rsKame was incubated in serum-free medium overnight and treated with 10 μM wortmannin for 1 h. The cells were then stimulated with or without 20 nM EGF for 1 min. Phosphorylated AKT was detected with an anti-phospho-AKT (Ser473) antibody in a western blotting analysis. Relative intensity was normalized to the mean value of the control cells without EGF stimulation. Data are means ± SD of three experiments.
(**B**) Effect of DN PLCγ on DAG production. DN PLCγ was transiently expressed in a cell line stably expressing EGFR–rsKame. Cells were incubated in serum-free medium overnight and treated with or without 20 nM EGF for 1 min. Amounts of DAG were measured with a DAG assay kit. Relative intensity was normalized to the mean intensity of the control cells without EGF stimulation. Data are means ± SD of three experiments.
(**C**) Bivariate H(r) value of EGFR–rsKame and PAmCherry–PI(4,5)P_2 in control (red), wortmannin-treated (green), and DN-PLCγ-expressing cells (black) after incubation with 20 nM EGF for 1 min. In control and wortmannin-treated cells, PAmCherry1–PLCδ-PH was transiently expressed in a cell line stably expressing EGFR–rsKame. To co-express PAmCherry1–PLCδ-PH and DN PLCγ in the same cells, plasmid DEST40/PAmCherry1–

PLCδ-PH–IRES–DN PLCγ was transfected to the cell line stably expressing EGFR–rsKame. Cells were incubated in serum-free medium overnight and treated with (control and DN PLCγ) or without 10 μM wortmannin for 1 h (wortmannin). The cells were then stimulated with 20 nM EGF for 1 min and treated with paraformaldehyde and glutaraldehyde. Data are means ± SEM of seven (control and wortmannin) or eight cells (DN PLCγ).

(**D**) Bivariate H(r) value of PAmCherry–PI(4,5)P_2 and HMSiR–pY1068 in control (red), wortmannin-treated (green), and DN-PLCγ-expressing cells (black) after incubation with 20 nM EGF for 1 min. After cells were prepared as described in (E), phosphorylated EGFR was immunostained with anti-EGFR (pY1068) and HMSiR-labeled antibodies. Data are means ± SEM of six (control), seven (wortmannin), or eight cells (DN PLCγ).

(**E**) Images of PAmCherry–PI(4,5)P_2 (magenta) and HMSiR-labeled pY1068 EGFR (yellow) after stimulation with EGF for 1 min. Cells were prepared as described in (F). **$p < 0.01$, ***$p < 0.001$ on Welch's *t* test.

Figure 7 Thr654 of EGFR is phosphorylated in a PLCγ-dependent manner.

(**A**) Effect of PLCγ on phosphorylation of EGFR. After EGFR-KO cells were transfected with EGFR–Halo, EGFR–Halo and DN PLCγ, or EGFR–Halo and PLCG1 siRNA, the cells were incubated in serum-free medium overnight and stimulated with 10 nM EGF for 1 min or 5 min. DN PLCγ was transiently expressed in EGFR-KO cells expressing EGFR–Halo. Phosphorylated-Tyr1068 EGFR, phosphorylated-Thr654 EGFR, and total EGFR were detected with anti-EGFR pY1068, anti-EGFR pT654, and anti-EGFR antibodies, respectively.

(**B**) Ratios of phosphorylated-Tyr1068 EGFR/total EGFR and phosphorylated-Thr654 EGFR/total EGFR. The ratios were normalized to the mean value of lane #7 in (A). Data are means ± SD of three experiments.

(**C**) Effects of AG1478 and PMA on phosphorylation of EGFR. After EGFR-KO cells were transfected with EGFR–Halo or EGFR–Halo and PLCG1 siRNA, the cells were incubated

in serum-free medium overnight and stimulated with 10 nM EGF for 5 min in the presence or absence of 100 nM PMA. For inhibition of autophosphorylation of EGFR, cells were treated with 1 μM AG1478 for 30 min and stimulated with 10 nM EGF for 5 min. Phosphorylated-Tyr1068 EGFR, phosphorylated-Thr654 EGFR, and total EGFR were detected with anti-EGFR pY1068, anti-EGFR pT654, and anti-EGFR antibodies, respectively.

(**D**) Ratios of phosphorylated-Tyr1068 EGFR/total EGFR and phosphorylated-Thr654 EGFR/total EGFR. The ratios were normalized to the mean value of lane #1 in (C). Data are means ± SD of three experiments.

(**E**) Schematic model of the activation and signal transduction process for EGFR. Left, after EGF stimulation, PI(4,5)P_2 (magenta) interacts with the arginine residues in the JM-A region (red) of EGFR, stabilizing the JM-A antiparallel dimer, and inducing the formation of asymmetric dimers of the kinase region (green) of EGFR. This dimerization results in the phosphorylation of several tyrosine residues in the tail region of EGFR. Right, Phosphorylated-Tyr1068 EGFR recruits PLCγ (yellow), degrading PI(4,5)P_2 and producing DAG. DAG activates protein kinase C (cyan), which phosphorylates Thr654 of EGFR, deactivating EGFR. *$p < 0.05$, **$p < 0.01$, NS (not significant) on Welch's *t* test.

References

Abd Halim, K.B., H. Koldsø, and M.S.P. Sansom. 2015. Interactions of the EGFR juxtamembrane domain with PIP2-containing lipid bilayers: Insights from multiscale molecular dynamics simulations. *Biochim Biophys Acta*. 1850:1017-1025.

Abe, M., A. Makino, F. Hullin-Matsuda, K. Kamijo, Y. Ohno-Iwashita, K. Hanada, H. Mizuno, A. Miyawaki, and T. Kobayashi. 2012. A role for sphingomyelin-rich lipid domains in the accumulation of phosphatidylinositol-4,5-bisphosphate to the cleavage furrow during cytokinesis. *Mol Cell Biol*. 32:1396-1407.

An, S.J., A. Anneken, Z. Xi, C. Choi, J. Schlessinger, and D. Toomre. 2022. Regulation of EGF-stimulated activation of the PI-3K/AKT pathway by exocyst-mediated exocytosis. *Proc Natl Acad Sci U S A*. 119:e2208947119.

Arkhipov, A., Y. Shan, R. Das, N.F. Endres, M.P. Eastwood, D.E. Wemmer, J. Kuriyan, and D.E. Shaw. 2013. Architecture and membrane interactions of the EGF receptor. *Cell*. 152:557-569.

Banan, A., J.Z. Fields, Y. Zhang, and A. Keshavarzian. 2001. Phospholipase C-gamma inhibition prevents EGF protection of intestinal cytoskeleton and barrier against oxidants. *Am J Physiol Gastrointest Liver Physiol*. 281:G412-423.

Berditchevski, F., and E. Odintsova. 2016. ErbB receptors and tetraspanins: Casting the net wider. *Int J Biochem Cell Biol*. 77:68-71.

Brown, D.A., and E. London. 1998. Functions of lipid rafts in biological membranes. *Annu Rev Cell Dev Biol*. 14:111-136.

Carpenter, G., and Q. Ji. 1999. Phospholipase C-gamma as a signal-transducing element. *Exp Cell Res*. 253:15-24.

Chen, X., and M.D. Resh. 2002. Cholesterol depletion from the plasma membrane triggers ligand-independent activation of the epidermal growth factor receptor. *J Biol Chem*. 277:49631-49637.

Endres, N.F., R. Das, A.W. Smith, A. Arkhipov, E. Kovacs, Y. Huang, J.G. Pelton, Y. Shan, D.E. Shaw, D.E. Wemmer, J.T. Groves, and J. Kuriyan. 2013. Conformational coupling across the plasma membrane in activation of the EGF receptor. *Cell*. 152:543-556.

Field, S.J., N. Madson, M.L. Kerr, K.A. Galbraith, C.E. Kennedy, M. Tahiliani, A. Wilkins, and L.C. Cantley. 2005. PtdIns(4,5)P2 functions at the cleavage furrow during cytokinesis. *Curr Biol*. 15:1407-1412.

Halova, I., and P. Draber. 2016. Tetraspanins and Transmembrane Adaptor Proteins As Plasma Membrane Organizers-Mast Cell Case. *Front Cell Dev Biol*. 4:43.

Hedger, G., M.S. Sansom, and H. Koldsø. 2015. The juxtamembrane regions of human receptor tyrosine kinases exhibit conserved interaction sites with anionic lipids. *Sci Rep*. 5:9198.

Hellyer, N.J., K. Cheng, and J.G. Koland. 1998. ErbB3 (HER3) interaction with the p85 regulatory subunit of phosphoinositide 3-kinase. *Biochem J*. 333 (Pt 3):757-763.

Hiroshima, M., C.G. Pack, K. Kaizu, K. Takahashi, M. Ueda, and Y. Sako. 2018. Transient Acceleration of Epidermal Growth Factor Receptor Dynamics Produces Higher-Order Signaling Clusters. *J Mol Biol*. 430:1386-1401.

Homma, Y., and T. Takenawa. 1992. Inhibitory effect of src homology (SH) 2/SH3 fragments of phospholipase C-gamma on the catalytic activity of phospholipase C isoforms. Identification of a novel phospholipase C inhibitor region. *J Biol Chem*. 267:21844-21849.

Hope, H.R., and L.J. Pike. 1996. Phosphoinositides and phosphoinositide-utilizing enzymes in detergent-insoluble lipid domains. *Mol Biol Cell*. 7:843-851.

Hunter, T., N. Ling, and J.A. Cooper. 1984. Protein kinase C phosphorylation of the EGF receptor at a threonine residue close to the cytoplasmic face of the plasma membrane. *Nature*. 311:480-483.

Insall, R.H., and O.D. Weiner. 2001. PIP3, PIP2, and cell movement--similar messages, different meanings? *Dev Cell*. 1:743-747.

Ji, Q.S., S. Ermini, J. Baulida, F.L. Sun, and G. Carpenter. 1998. Epidermal growth factor signaling and mitogenesis in Plcg1 null mouse embryonic fibroblasts. *Mol Biol Cell*. 9:749-757.

Jura, N., N.F. Endres, K. Engel, S. Deindl, R. Das, M.H. Lamers, D.E. Wemmer, X. Zhang, and J. Kuriyan. 2009a. Mechanism for activation of the EGF receptor catalytic domain by the juxtamembrane segment. *Cell*. 137:1293-1307.

Jura, N., Y. Shan, X. Cao, D.E. Shaw, and J. Kuriyan. 2009b. Structural analysis of the catalytically inactive kinase domain of the human EGF receptor 3. *Proc Natl Acad Sci U S A*. 106:21608-21613.

Ketel, K., M. Krauss, A.S. Nicot, D. Puchkov, M. Wieffer, R. Müller, D. Subramanian, C. Schultz, J. Laporte, and V. Haucke. 2016. A phosphoinositide conversion mechanism for exit from endosomes. *Nature*. 529:408-412.

Kiskowski, M.A., J.F. Hancock, and A.K. Kenworthy. 2009. On the use of Ripley's K-function and its derivatives to analyze domain size. *Biophys J*. 97:1095-1103.

Kuwashima, Y., M. Yanagawa, M. Abe, M. Hiroshima, M. Ueda, M. Arita, and Y. Sako. 2021. Comparative Analysis of Single-Molecule Dynamics of TRPV1 and TRPV4 Channels in Living Cells. *Int J Mol Sci*. 22.

Lagache, T., A. Grassart, S. Dallongeville, O. Faklaris, N. Sauvonnet, A. Dufour, L. Danglot, and J.C. Olivo-Marin. 2018. Mapping molecular assemblies with fluorescence microscopy and object-based spatial statistics. *Nat Commun*. 9:698.

Laux, T., K. Fukami, M. Thelen, T. Golub, D. Frey, and P. Caroni. 2000. GAP43, MARCKS, and CAP23 modulate PI(4,5)P(2) at plasmalemmal rafts, and regulate cell cortex actin dynamics through a common mechanism. *J Cell Biol*. 149:1455-1472.

Lemmon, M.A., J. Schlessinger, and K.M. Ferguson. 2014. The EGFR family: not so prototypical receptor tyrosine kinases. *Cold Spring Harb Perspect Biol*. 6:a020768.

Liang, H., H. Mu, F. Jean-Francois, B. Lakshman, S. Sarkar-Banerjee, Y. Zhuang, Y. Zeng, W. Gao, A.M. Zaske, D.V. Nissley, A.A. Gorfe, W. Zhao, and Y. Zhou. 2019. Membrane curvature sensing of the lipid-anchored K-Ras small GTPase. *Life Sci Alliance*. 2.

Liu, J., R. van der Hoeven, W.E. Kattan, J.T. Chang, D. Montufar-Solis, W. Chen, M. Wong, Y. Zhou, C.B. Lebrilla, and J.F. Hancock. 2023. Glycolysis regulates KRAS plasma membrane localization and function through defined glycosphingolipids. *Nat Commun*. 14:465.

Maeda, R., T. Sato, K. Okamoto, M. Yanagawa, and Y. Sako. 2018. Lipid-Protein Interplay in Dimerization of Juxtamembrane Domains of Epidermal Growth Factor Receptor. *Biophys J*. 114:893-903.

Maeda, R., H. Tamagaki-Asahina, T. Sato, M. Yanagawa, and Y. Sako. 2022. Threonine phosphorylation regulates the molecular assembly and signaling of EGFR in cooperation with membrane lipids. *J Cell Sci*. 135.

Makino, A., M. Abe, R. Ishitsuka, M. Murate, T. Kishimoto, S. Sakai, F. Hullin-Matsuda, Y. Shimada, T. Inaba, H. Miyatake, H. Tanaka, A. Kurahashi, C.G. Pack, R.S. Kasai, S. Kubo, N.L. Schieber, N. Dohmae, N. Tochio, K. Hagiwara, Y. Sasaki, Y. Aida, F. Fujimori, T. Kigawa, K. Nishibori, R.G. Parton, A. Kusumi, Y. Sako, G. Anderluh, M. Yamashita, T. Kobayashi, P. Greimel, and T. Kobayashi. 2017. A novel sphingomyelin/cholesterol domain-specific probe reveals the dynamics of the membrane domains during virus release and in Niemann-Pick type C. *FASEB J*. 31:1301-1322.

Malek, M., A. Kielkowska, T. Chessa, K.E. Anderson, D. Barneda, P. Pir, H. Nakanishi, S. Eguchi, A. Koizumi, J. Sasaki, V. Juvin, V.Y. Kiselev, I. Niewczas, A. Gray, A. Valayer, D. Spensberger, M. Imbert, S. Felisbino, T. Habuchi, S. Beinke, S. Cosulich, N. Le Novère, T. Sasaki, J. Clark,

P.T. Hawkins, and L.R. Stephens. 2017. PTEN Regulates PI(3,4)P(2) Signaling Downstream of Class I PI3K. *Mol Cell*. 68:566-580.e510.

Matsushita, C., H. Tamagaki, Y. Miyazawa, S. Aimoto, S.O. Smith, and T. Sato. 2013. Transmembrane helix orientation influences membrane binding of the intracellular juxtamembrane domain in Neu receptor peptides. *Proc Natl Acad Sci U S A*. 110:1646-1651.

Mattoon, D.R., B. Lamothe, I. Lax, and J. Schlessinger. 2004. The docking protein Gab1 is the primary mediator of EGF-stimulated activation of the PI-3K/Akt cell survival pathway. *BMC Biol*. 2:24.

McLaughlin, S., S.O. Smith, M.J. Hayman, and D. Murray. 2005. An electrostatic engine model for autoinhibition and activation of the epidermal growth factor receptor (EGFR/ErbB) family. *J Gen Physiol*. 126:41-53.

Nieuwenhuizen, R.P., K.A. Lidke, M. Bates, D.L. Puig, D. Grünwald, S. Stallinga, and B. Rieger. 2013. Measuring image resolution in optical nanoscopy. *Nat Methods*. 10:557-562.

Nyati, M.K., M.A. Morgan, F.Y. Feng, and T.S. Lawrence. 2006. Integration of EGFR inhibitors with radiochemotherapy. *Nat Rev Cancer*. 6:876-885.

Odintsova, E., J. Voortman, E. Gilbert, and F. Berditchevski. 2003. Tetraspanin CD82 regulates compartmentalisation and ligand-induced dimerization of EGFR. *J Cell Sci*. 116:4557-4566.

Ogiso, H., R. Ishitani, O. Nureki, S. Fukai, M. Yamanaka, J.H. Kim, K. Saito, A. Sakamoto, M. Inoue, M. Shirouzu, and S. Yokoyama. 2002. Crystal structure of the complex of human epidermal growth factor and receptor extracellular domains. *Cell*. 110:775-787.

Olayioye, M.A., R.M. Neve, H.A. Lane, and N.E. Hynes. 2000. The ErbB signaling network: receptor heterodimerization in development and cancer. *Embo j*. 19:3159-3167.

Pujals, S., N. Feiner-Gracia, P. Delcanale, I. Voets, and L. Albertazzi. 2019. Super-resolution microscopy as a powerful tool to study complex synthetic materials. *Nature Reviews Chemistry*. 3:68-84.

Ran, F.A., P.D. Hsu, J. Wright, V. Agarwala, D.A. Scott, and F. Zhang. 2013. Genome engineering using the CRISPR-Cas9 system. *Nat Protoc*. 8:2281-2308.

Red Brewer, M., S.H. Choi, D. Alvarado, K. Moravcevic, A. Pozzi, M.A. Lemmon, and G. Carpenter. 2009. The juxtamembrane region of the EGF receptor functions as an activation domain. *Mol Cell*. 34:641-651.

Ringerike, T., F.D. Blystad, F.O. Levy, I.H. Madshus, and E. Stang. 2002. Cholesterol is important in control of EGF receptor kinase activity but EGF receptors are not concentrated in caveolae. *J Cell Sci*. 115:1331-1340.

Rosenbloom, A.B., S.H. Lee, M. To, A. Lee, J.Y. Shin, and C. Bustamante. 2014. Optimized two-color super resolution imaging of Drp1 during mitochondrial fission with a slow-switching Dronpa variant. *Proc Natl Acad Sci U S A*. 111:13093-13098.

Rust, M.J., M. Bates, and X. Zhuang. 2006. Sub-diffraction-limit imaging by stochastic optical reconstruction microscopy (STORM). *Nat Methods*. 3:793-795.

Sako, Y., S. Minoghchi, and T. Yanagida. 2000. Single-molecule imaging of EGFR signalling on the surface of living cells. *Nat Cell Biol*. 2:168-172.

Steinberg, S.F. 2008. Structural basis of protein kinase C isoform function. *Physiol Rev*. 88:1341-1378.

Sugiyama, M.G., A.I. Brown, J. Vega-Lugo, J.P. Borges, A.M. Scott, K. Jaqaman, G.D. Fairn, and C.N. Antonescu. 2023. Confinement of unliganded EGFR by tetraspanin nanodomains gates EGFR ligand binding and signaling. *Nat Commun*. 14:2681.

Takakura, H., Y. Zhang, R.S. Erdmann, A.D. Thompson, Y. Lin, B. McNellis, F. Rivera-Molina, S.N. Uno, M. Kamiya, Y. Urano, J.E. Rothman, J. Bewersdorf, A. Schepartz, and D. Toomre. 2017. Long time-lapse nanoscopy with spontaneously blinking membrane probes. *Nat Biotechnol*. 35:773-780.

Thiel, K.W., and G. Carpenter. 2007. Epidermal growth factor receptor juxtamembrane region regulates allosteric tyrosine kinase activation. *Proc Natl Acad Sci U S A*. 104:19238-19243.

Uchida, Y., J. Hasegawa, D. Chinnapen, T. Inoue, S. Okazaki, R. Kato, S. Wakatsuki, R. Misaki, M. Koike, Y. Uchiyama, S. Iemura, T. Natsume, R. Kuwahara, T. Nakagawa, K. Nishikawa, K. Mukai, E. Miyoshi, N. Taniguchi, D. Sheff, W.I. Lencer, T. Taguchi, and H. Arai. 2011. Intracellular phosphatidylserine is essential for retrograde membrane traffic through endosomes. *Proc Natl Acad Sci U S A*. 108:15846-15851.

Wagner, M.J., M.M. Stacey, B.A. Liu, and T. Pawson. 2013. Molecular mechanisms of SH2- and PTB-domain-containing proteins in receptor tyrosine kinase signaling. *Cold Spring Harb Perspect Biol*. 5:a008987.

Wells, A. 1999. EGF receptor. *Int J Biochem Cell Biol*. 31:637-643.

Yanagawa, M., M. Hiroshima, Y. Togashi, M. Abe, T. Yamashita, Y. Shichida, M. Murata, M. Ueda, and Y. Sako. 2018. Single-molecule diffusion-based estimation of ligand effects on G protein-coupled receptors. *Sci Signal*. 11.

Yanagawa, M., and Y. Sako. 2021. Workflows of the Single-Molecule Imaging Analysis in Living Cells: Tutorial Guidance to the Measurement of the Drug Effects on a GPCR. *Methods Mol Biol*. 2274:391-441.

Yano, H., S. Nakanishi, K. Kimura, N. Hanai, Y. Saitoh, Y. Fukui, Y. Nonomura, and Y. Matsuda. 1993. Inhibition of histamine secretion by wortmannin through the blockade of phosphatidylinositol 3-kinase in RBL-2H3 cells. *J Biol Chem*. 268:25846-25856.

Yasui, M., M. Hiroshima, J. Kozuka, Y. Sako, and M. Ueda. 2018. Automated single-molecule imaging in living cells. *Nat Commun*. 9:3061.

Yoshizawa, R., N. Umeki, A. Yamamoto, M. Okada, M. Murata, and Y. Sako. 2021. p52Shc regulates the sustainability of ERK activation in a RAF-independent manner. *Mol Biol Cell*. 32:1838-1848.

Zhang, X., J. Gureasko, K. Shen, P.A. Cole, and J. Kuriyan. 2006. An allosteric mechanism for activation of the kinase domain of epidermal growth factor receptor. *Cell*. 125:1137-1149.

Zhou, Y., H. Liang, T. Rodkey, N. Ariotti, R.G. Parton, and J.F. Hancock. 2014. Signal integration by lipid-mediated spatial cross talk between Ras nanoclusters. *Mol Cell Biol*. 34:862-876.

Zhou, Y., P. Prakash, H. Liang, K.J. Cho, A.A. Gorfe, and J.F. Hancock. 2017. Lipid-Sorting Specificity Encoded in K-Ras Membrane Anchor Regulates Signal Output. *Cell*. 168:239-251.e216.

Zhou, Y., C.O. Wong, K.J. Cho, D. van der Hoeven, H. Liang, D.P. Thakur, J. Luo, M. Babic, K.E. Zinsmaier, M.X. Zhu, H. Hu, K. Venkatachalam, and J.F. Hancock. 2015. SIGNAL TRANSDUCTION. Membrane potential modulates plasma membrane phospholipid dynamics and K-Ras signaling. *Science*. 349:873-876.

Abe et al., Figure 1

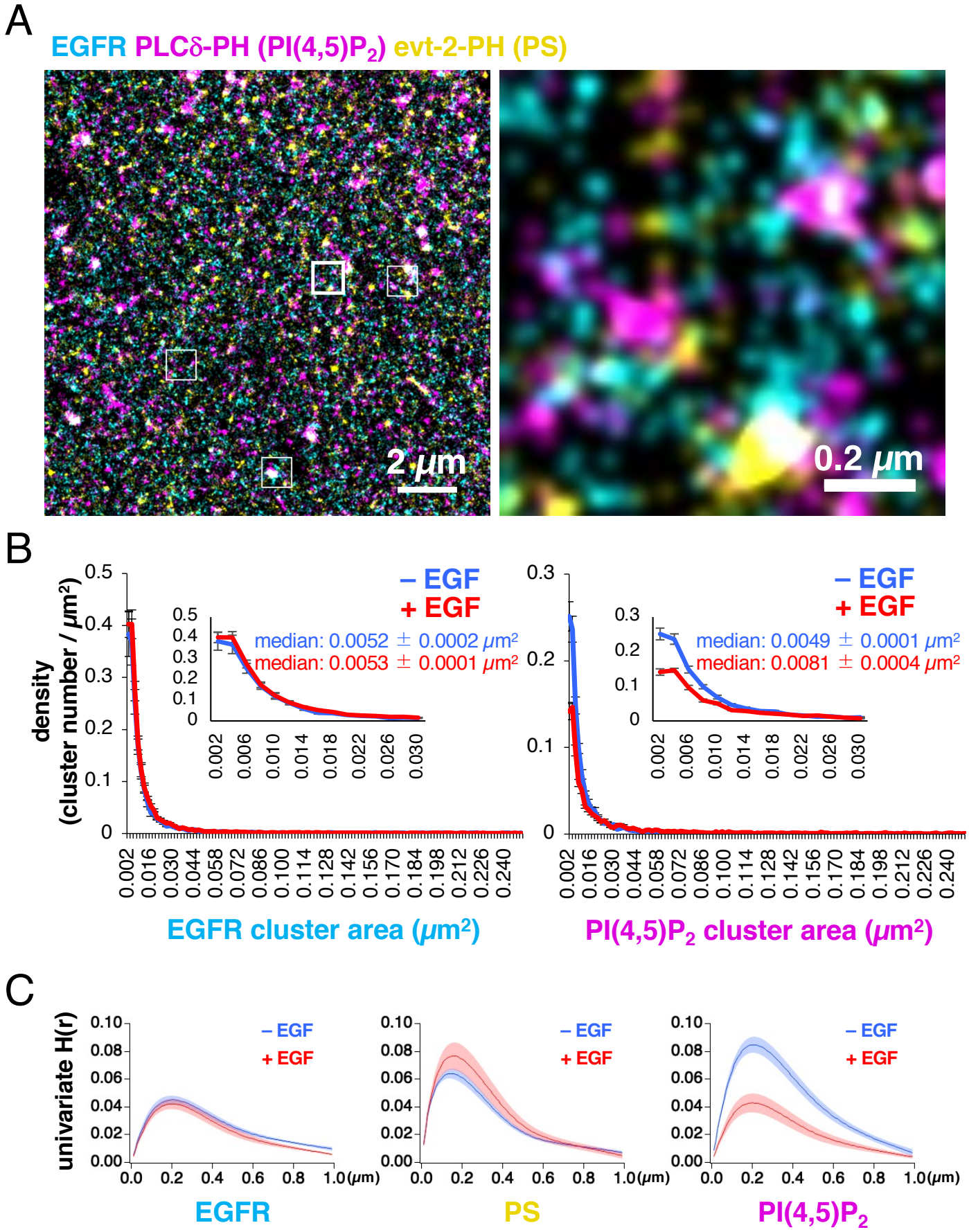

Abe et al., Figure 2

A

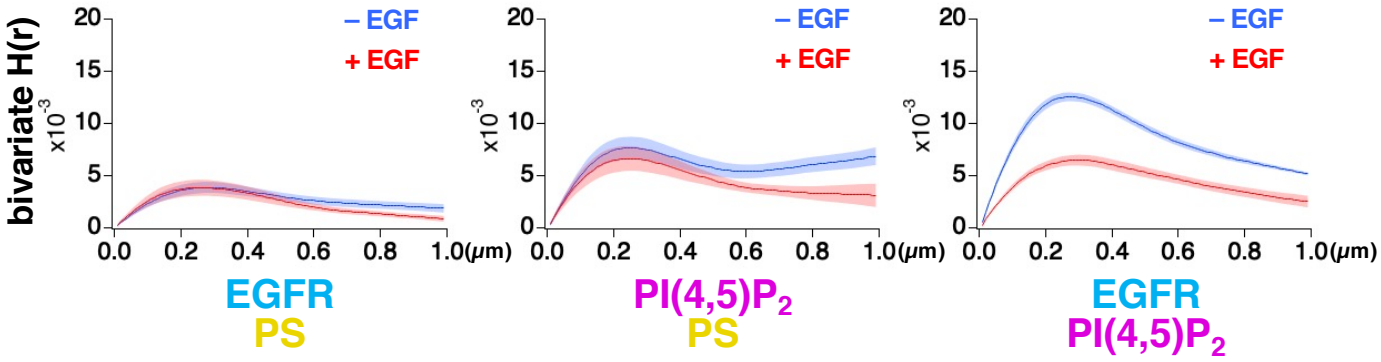

B

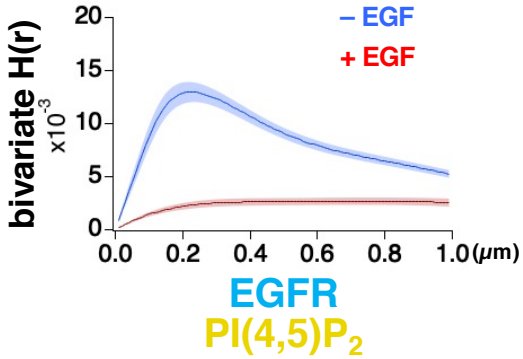

C

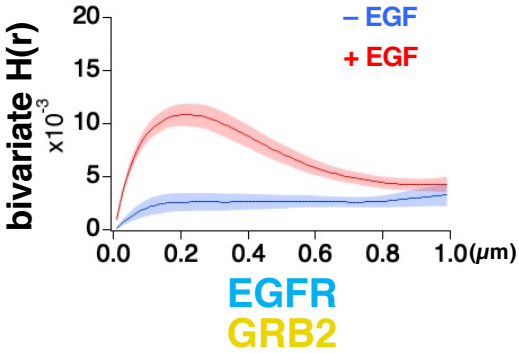

D

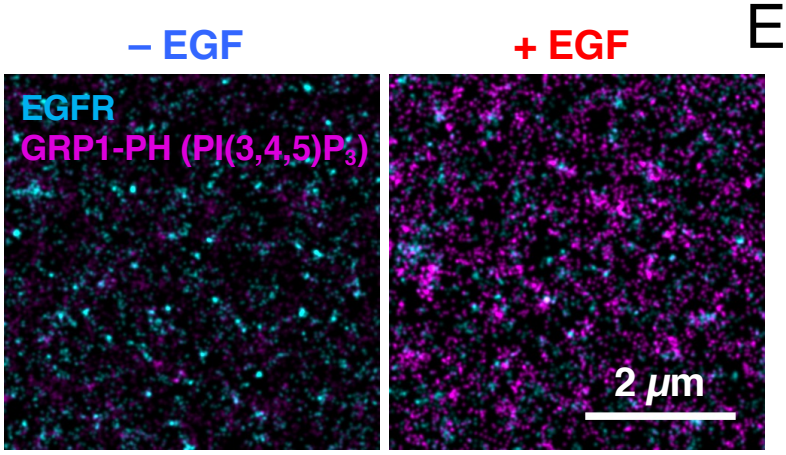

E

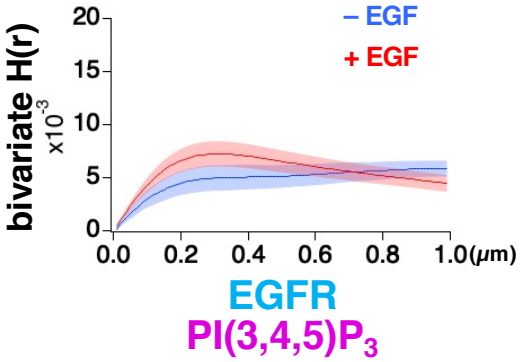

Abe et al., Figure 3

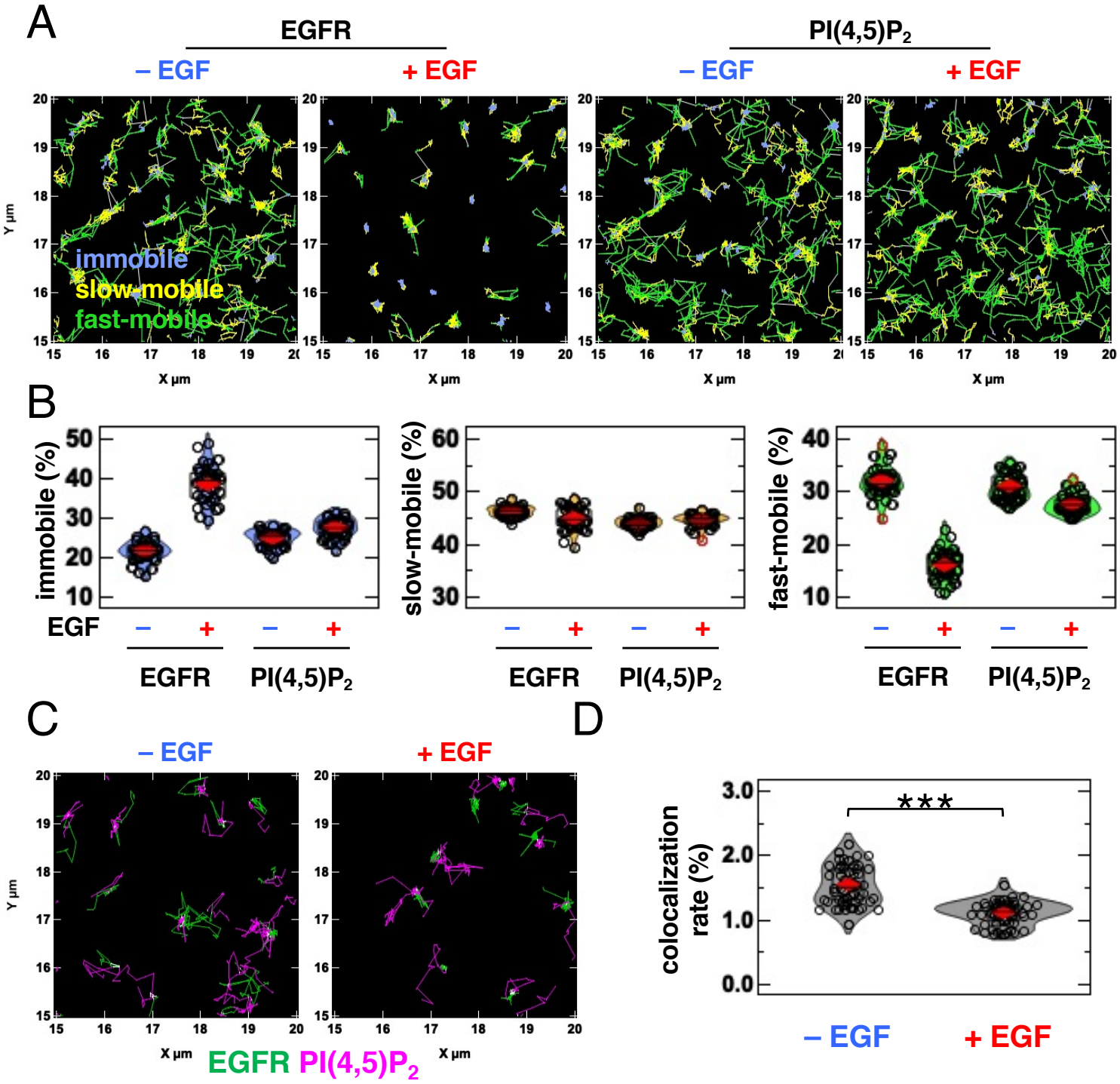

Abe et al., Figure 4

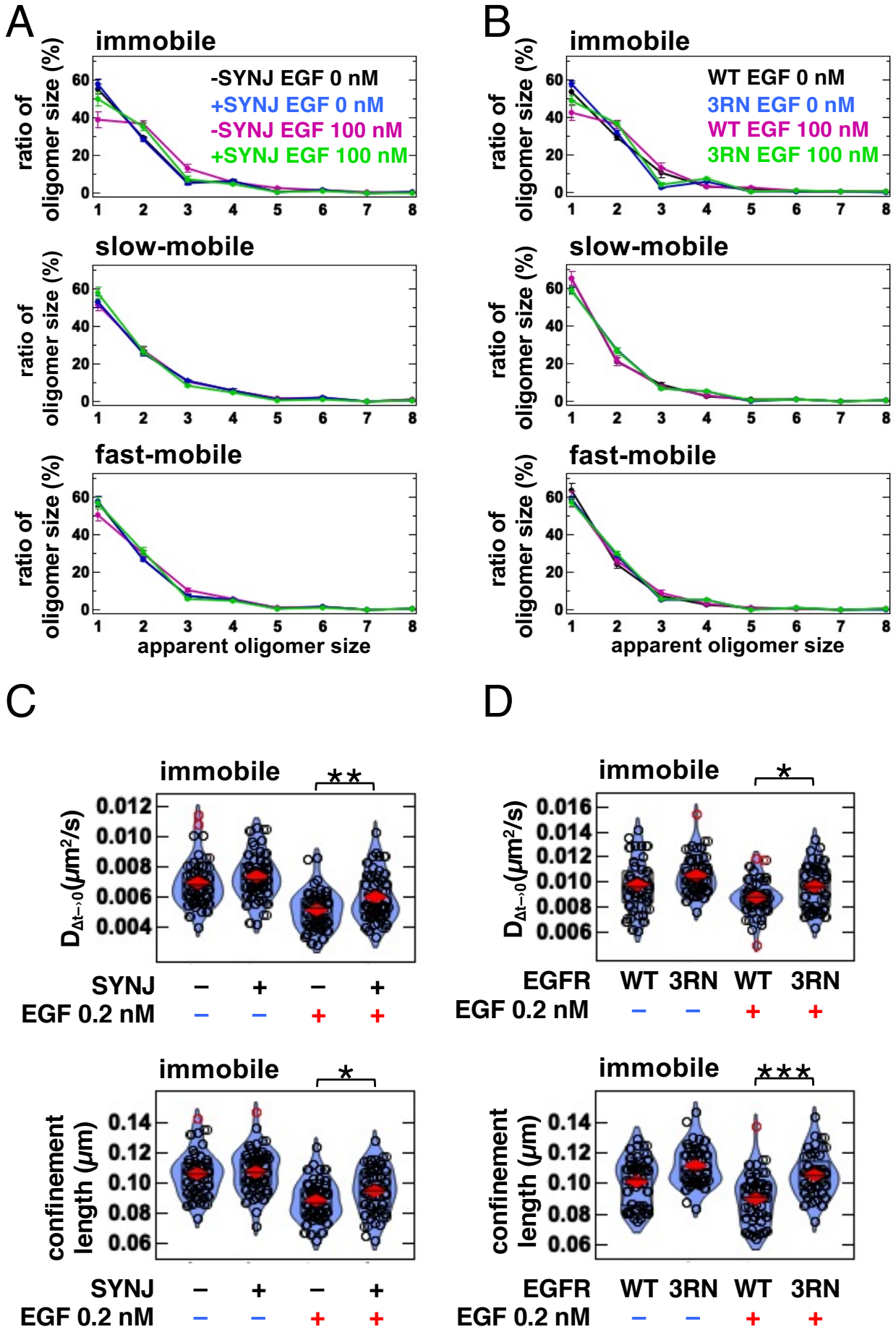

Abe et al., Figure 5

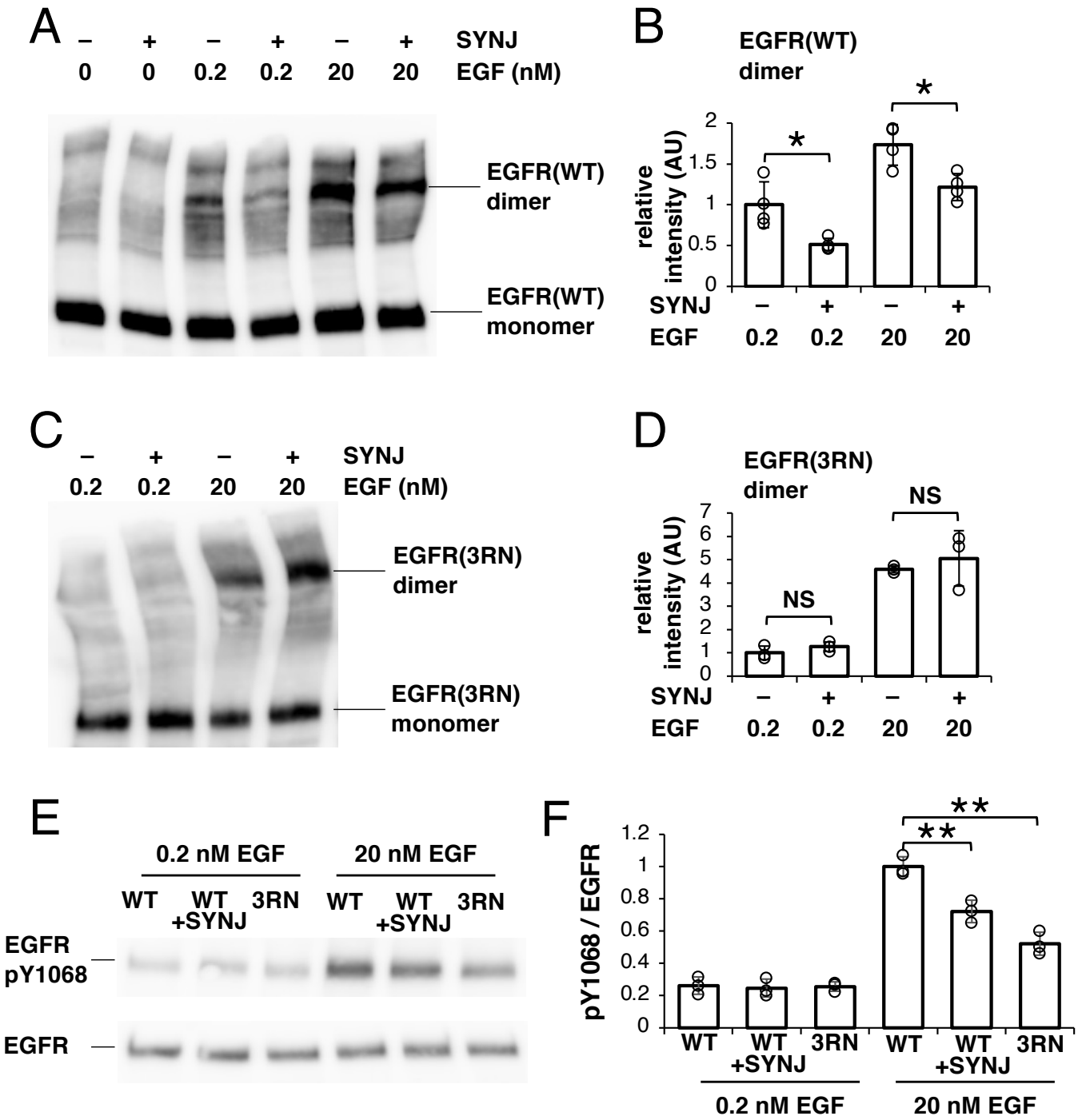

Abe et al., Figure 6

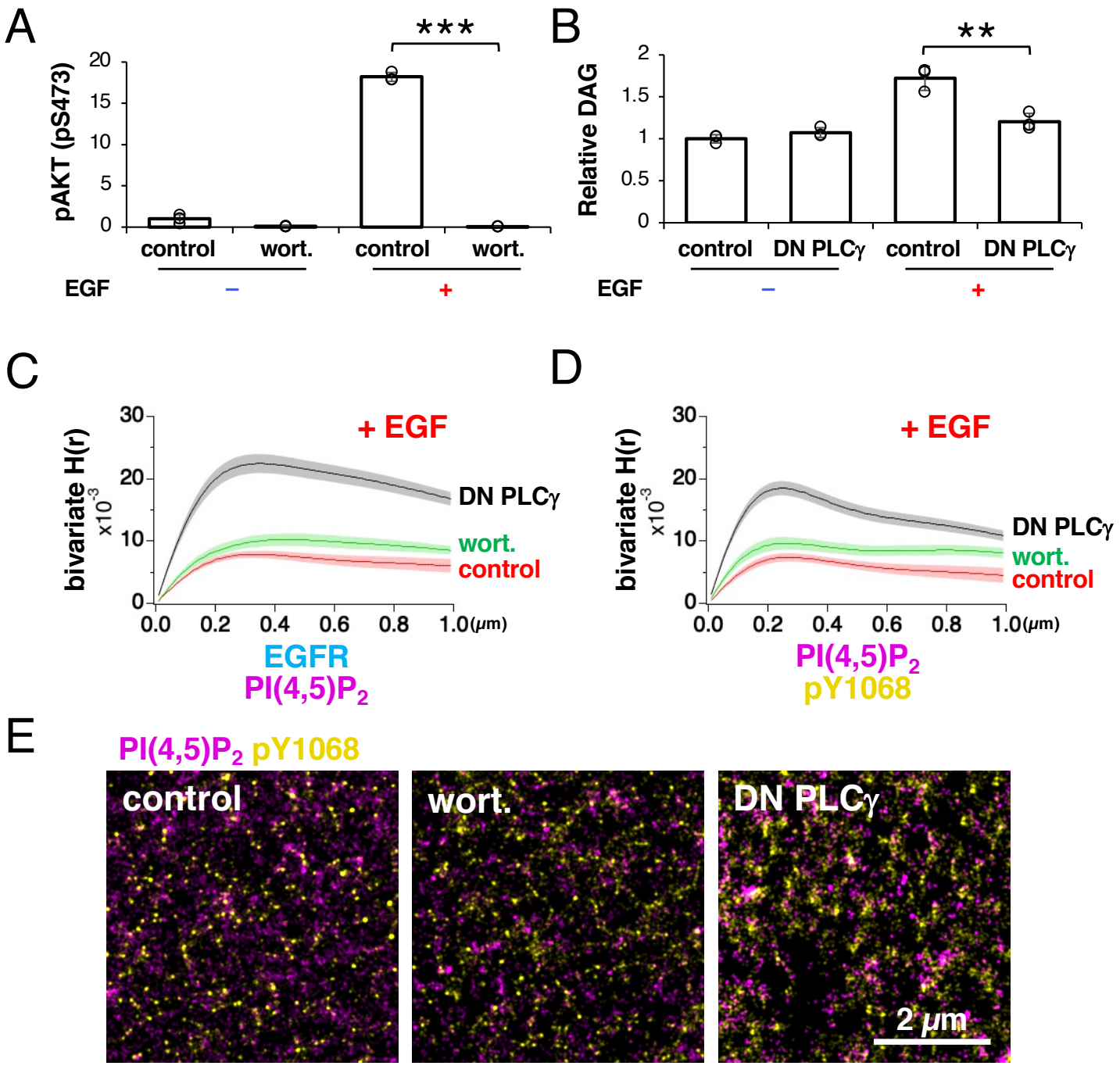
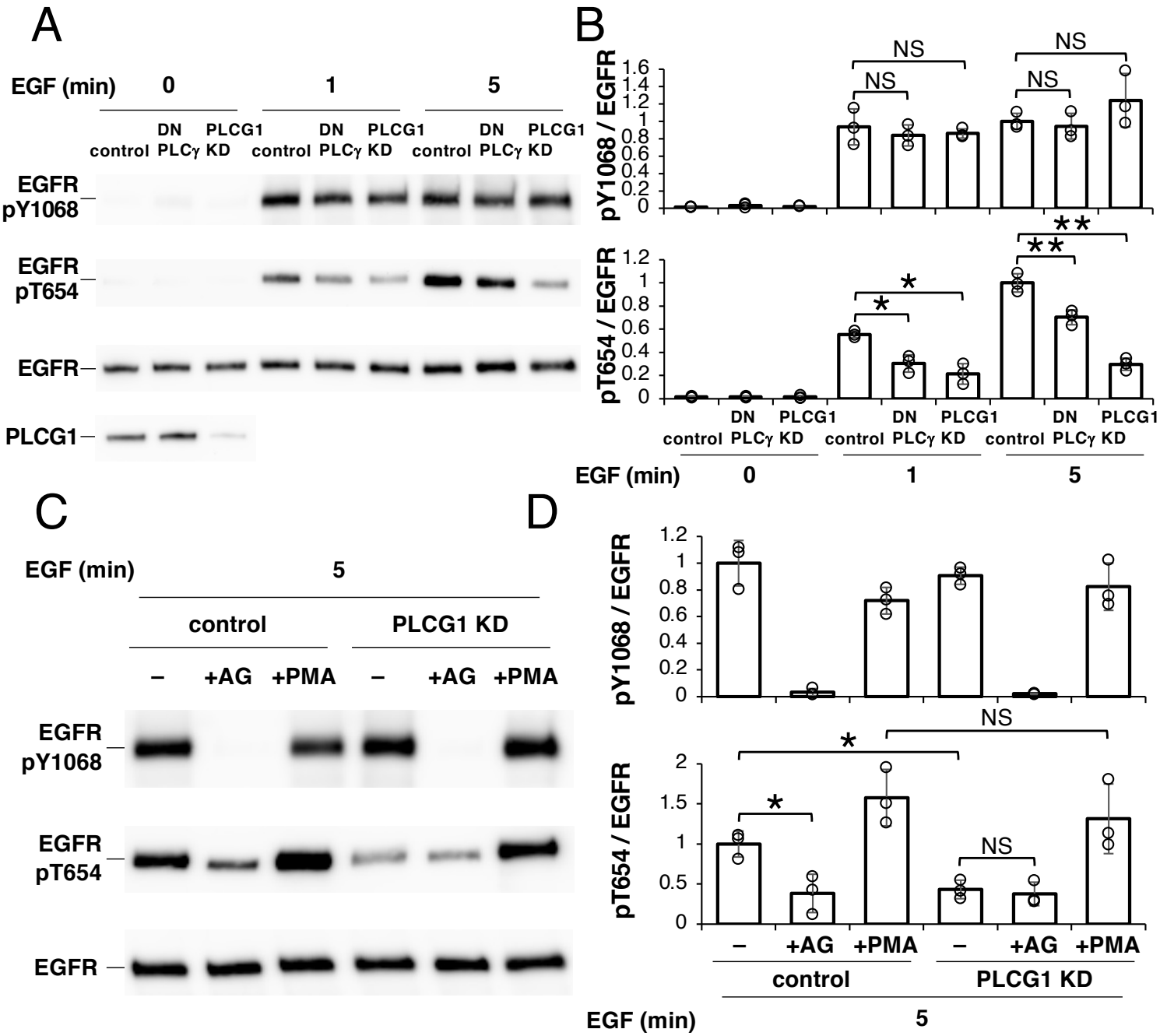
Abe et al., Figure 7